

RESEARCH ARTICLE | JUNE 26 2024

Dynamics of a cavitation bubble confined in a thin liquid layer at null Kelvin impulse

Jure Zevnik ; Julien Patfoort ; Juan Manuel Rosselló ; Claus-Dieter Ohl ; Matevž Dular 



Physics of Fluids 36, 063340 (2024)

<https://doi.org/10.1063/5.0209287>



Articles You May Be Interested In

Investigation on laser-induced bubble collapse among triple particles based on high-frame-rate photography and the Kelvin impulse model

Physics of Fluids (May 2024)

Microbubble collapse near a fiber: Broken symmetry conditions and a planar jet formation

Physics of Fluids (February 2023)

The evolution of the bubble collapse morphology between two cylinders within a confined space

Physics of Fluids (October 2024)



Physics of Fluids

Special Topics Open
for Submissions

[Learn More](#)

Dynamics of a cavitation bubble confined in a thin liquid layer at null Kelvin impulse

Cite as: Phys. Fluids **36**, 063340 (2024); doi: [10.1063/5.0209287](https://doi.org/10.1063/5.0209287)

Submitted: 20 March 2024 · Accepted: 2 June 2024 ·

Published Online: 26 June 2024



View Online



Export Citation



CrossMark

Jure Zevnik,^{1,a)} Julien Patfoort,² Juan Manuel Rosselló,¹ Claus-Dieter Ohl,³ and Matevž Dular¹

AFFILIATIONS

¹Faculty of Mechanical Engineering, University of Ljubljana, Aškerčeva cesta 6, Ljubljana, Slovenia

²Polytechnic Institute of Bordeaux, Av. des Facultés, 33405 Talence, France

³Institute of Physics, Otto von Guericke University Magdeburg, Universitätplatz 2, Magdeburg, Germany

^{a)} Author to whom correspondence should be addressed: jure.zevnik@fs.uni-lj.si

ABSTRACT

In this work, we experimentally and numerically investigate cavitation bubble dynamics in a thin liquid layer surrounded by gas. We focus on configurations featuring strongly confined bubbles at dimensionless bubble-free surface stand-off distances D^* below unity. Additionally, we impose the condition of null Kelvin impulse, subjecting a bubble to the oppositely equal influence of two opposing free surfaces, resulting in the formation of two convergent water jets. We observe a diverse spectrum of jetting phenomena, including broad jets, mushroom-capped jets, and cylindrical jets. These jets become progressively thinner and faster with lower D^* values, reaching radii as small as 3% of the maximal bubble radius and speeds up to 150 m/s. Numerical results reveal a linear relationship between the jet impact velocity and the local curvature at the bubble region proximal to the free surface. This suggests that the magnitude of bubble deformation during its growth phase is the primary factor influencing the observed fivefold increase in the jet impact velocity in the parameter space considered. Our findings show that bubble collapse intensity is progressively dampened with increased confinement of its environment. As D^* decreases beyond a critical value, the liquid layer separating the bubble and ambient air thins, leading to the onset of interfacial shape instabilities, its breakdown, and bubble atomization. Furthermore, we compare bubbles at zero Kelvin impulse to corresponding anisotropic scenarios with a single free surface, revealing that the dynamics of axial jets until the time of impact is primarily influenced by the proximal free surface. The impact of convergent axial jets at null Kelvin impulse results in local pressure transients up to 100 MPa and triggers the formation of a fast and thin annular outflow in the form of a liquid sheet, affected by the Rayleigh–Plateau and flapping shape instability.

© 2024 Author(s). All article content, except where otherwise noted, is licensed under a Creative Commons Attribution (CC BY) license (<https://creativecommons.org/licenses/by/4.0/>). <https://doi.org/10.1063/5.0209287>

I. INTRODUCTION

Cavitation is a phenomenon where a sudden decrease in pressure triggers the formation of vapor and gas bubbles inside a liquid medium. These gaseous structures are unstable and often implode violently, i.e., collapse, when they encounter a region of increased pressure. Generally, two types of cavitation are distinguished: acoustic and hydrodynamic cavitation, depending on the origin of the pressure decrease. However, cavitation can also occur due to laser-induced optical breakdown in liquids, which results in plasma formation that leads to bubble formation, its explosive growth, and subsequent implosion.

Research on cavitation bubbles and their collapse dynamics was primarily pursued due to the undesirable consequences of cavitation, such as material erosion and vibrations in hydraulic machinery and ship propellers.¹ However, today's research extends far beyond that, as cavitation is being utilized in the fields of medicine,^{2,3} chemistry,^{4,5} environmental protection,^{6,7} and engineering.^{8,9} Most processes exploit

cavitation for a beneficial outcome, such as enhancing the emulsification process, which results from the extreme conditions that accompany cavitation and bubble implosions. These effects generally fall into two main categories: mechanical and chemical. Mechanical effects include water jets,^{10,11} strong shear flows,^{12,13} high local temperatures,^{14,15} and shock waves.^{16,17} Chemical effects arise from the highly reactive free radicals formed during strong bubble implosions.^{18,19} Similar considerations apply in engineering and medical applications where the aim is to mitigate the damaging consequences of these effects, such as preventing material erosion or unwanted tissue damage due to shock waves and water jet impact.

Decades of research on cavitation bubble dynamics have revealed that when bubbles are exposed to anisotropic environments, e.g., near walls^{20,21} or free surfaces,^{22,23} in the vicinity of other bubbles²⁴ and bacterial cells,¹³ or in the presence of an acoustic field,²⁵ their shapes can deviate significantly from the idealized spherical one.^{26,27} A particularly

interesting and well-researched phenomenon is the formation of a liquid jet, which is a common result of non-spherical bubble collapse in various anisotropic environments. The liquid jet, also known as a micro jet, forms due to axial flow focusing and adopts a characteristic uniaxial shape. It has been identified as one of the key factors contributing to the potentially destructive nature of imploding bubbles, as these jets typically reach speeds on the order of 10–100 m/s and can induce high local pressures and shear stresses upon impact with nearby boundaries.^{12,28}

An often-encountered concept related to bubble dynamics is the so-called Kelvin impulse.^{1,29} It is defined as the momentum acquired by the ambient liquid during the growth and collapse of a bubble and has been shown to provide a valuable framework for understanding bubble dynamics.²⁶ Following the work of Blake,²⁹ Obreschkow *et al.*³⁰ proposed a dimensionless version of the Kelvin impulse:

$$\zeta = -\nabla p R_{\max} \Delta p^{-1}, \quad (1)$$

which is closely related to the anisotropy parameter $\zeta = |\zeta|$. Here, ∇p , R_{\max} , and Δp denote the pressure field gradient, the maximum radius attained by the bubble, and the bubble collapse driving pressure, respectively. The latter is defined as the difference between the far-field ambient pressure and vapor pressure. The anisotropy parameter can be understood as a measure of the anisotropy of the bubble environment and thus the onset of the phenomenon of bubble jetting.²⁷ Although the theory of Kelvin impulse is based on several assumptions that cease to be valid in highly anisotropic environments (e.g., neglecting possible deformation of boundaries), it can provide practical insight into engineering and industrial design problems.²⁶ Thus, ζ has been defined for some commonly considered anisotropic environments,³⁰ such as a flat free surface and a gravitational field. The anisotropy parameter in its vector form for the case of a flat free surface is defined as

$$\zeta = 0.195 \left(\frac{R_{\max}}{d} \right)^2 \mathbf{n}, \quad (2)$$

where d is the initial stand-off distance between the bubble center and the free surface, and \mathbf{n} is the unit normal vector at the free surface oriented toward the bubble. This definition implies a net momentum acquisition in the direction away from the free surface, which is consistent with the observed direction of bubble jetting when bubbles evolve near a free surface.²⁷

A plethora of research has addressed bubble dynamics and resulting jetting phenomena^{21,23,31–34} in various environments that encompass either a single or a combination of jet drivers. In the latter case, the net anisotropy parameter can be determined as a vector sum of the corresponding ζ for each present jet driver. Based on this, a condition of null Kelvin impulse thus does not only include an unbounded spherical bubble, but also a combination of jet drivers, where their relative contributions to anisotropic bubble collapse cancel out. However, this does not necessarily result in spherical bubble dynamics and can lead to bubble splitting and formation of equatorial jets.²⁶ While the implications of a net null Kelvin impulse environment on bubble dynamics have been addressed in the past, it was often pursued as a limiting case where the directionality of the overall bubble displacement and the resulting jetting phenomena changes, i.e., neutral bubble collapse. Researchers have thus far considered either stagnation

flow^{26,29,35,36} or a combination of buoyant forces counteracted by the effects of various boundaries, ranging from rigid and composite boundaries to free surfaces and liquid interfaces.^{26,29,35,37,38} An important consideration here is that the anisotropy parameter ζ in both gravitational fields and stationary potential flows is not scale-independent. Additionally, according to previous literature, the dynamics of bubble collapse and the characteristics of formed jets in the strong jetting regime ($\zeta > 0.1$) are highly dependent on the drivers of anisotropy.²⁷ Therefore, one can reasonably expect bubbles to behave uniquely in different strongly confined environments, even when the net Kelvin impulse amounts to zero.

We explore this concept within a paradigm wherein spherical bubble dynamics, often assumed in many applications, may be an over-idealization of the actual phenomena. Particularly, larger, macro-scaled bubbles are susceptible to variable ambient conditions and tend to deform, generate jets, or even fragment during their lifetime. Thus, achieving controlled and repetitive generation of perfectly spherical bubbles in many real-world conditions is challenging, at best. In this context, a strongly confined bubble environment can be understood as a controlled bubble environment, where resulting bubble dynamics are less influenced by uncontrollable factors. Such controlled environments could prove beneficial in processes that exploit cavitation and cavitation bubbles.

Boundaries, depending on their characteristics, can be viewed on a spectrum from bubble-attracting ($\zeta \cdot \mathbf{n} < 0$, e.g., a flat rigid surface) to bubble-repelling ($\zeta \cdot \mathbf{n} > 0$, e.g., a free surface). Including an additional criterion of null Kelvin impulse could provide further control over the net bubble displacement and resulting jets. For instance, a configuration of two parallel rigid surfaces typically results in divergent bubble dynamics with bubble splitting and the formation of axial jets toward each wall.^{39–41} In contrast, in the same geometric configuration with two free surfaces, a different outcome is expected. Due to the bubble-repelling nature of a water–air interface, one would anticipate convergent bubble dynamics with the formation of two opposing axial jets. In this scenario, there is a possibility of controlled energy focusing upon the impact of convergent axial jets. While bubble dynamics inside free-falling⁴² and turbulent⁴³ liquid jets have been studied in the past, to the best of our knowledge, bubble dynamics in a stagnant liquid layer bounded by two opposing free surfaces has not been researched yet. Another important distinction from the rigid wall case is that free surfaces can undergo severe deformation and even rupture^{23,44} when bubbles are initiated in close proximity to them.

Under the idealized assumption of a bubble between two parallel flat free-surfaces, two independent dimensionless parameters are needed to fully describe the geometric configuration of the phenomenon. We employ dimensionless distance from the bubble center (plasma spot centroid) to each free surface, such that $d_1 \leq d_2$ (Fig. 1). In the absence of other anisotropy drivers, a null Kelvin impulse condition enforces $d_1 = d_2$, and thus, we omit the subscripts, such that $d_1 = d_2 := d$. According to previous literature, there are multiple options for a characteristic bubble length to be considered. For consistency with similar literature, we use the parameter D^* as defined in Eq. (3), which employs the maximum radius R_{\max}^{unb} of an equivalent bubble in unbounded conditions as a scaling length.⁴⁵ Subscripts 1 and 2 are reintroduced only when comparing bubble dynamics at null Kelvin impulse to that in a corresponding anisotropic configuration, i.e., a single free surface scenario where $D_2^* = \infty$.

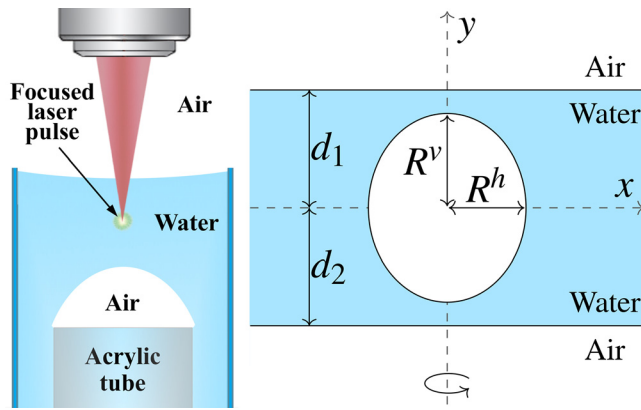


FIG. 1. A schematic representation of the experimental setup (left) and the considered phenomenon (right)—a bubble is induced in water between two opposing free surfaces.

$$D^* = \frac{d}{R_{\max}^{\text{unb}}} \quad (3)$$

After the introduction, Secs. II and III describe the experimental and numerical methods employed. Supplementary results for the case of a single unbounded numerical bubble are included to determine initial conditions, validate the newly employed methodology, and estimate the discretization errors for the selected spatiotemporal resolution of the simulations. Subsequently, the main results are presented and discussed, providing insight into a diverse spectrum of bubble dynamics and jetting phenomena observed when bubbles evolve in a strongly confined ($D^* \leq 1$) and symmetric environment comprising a thin liquid layer. Characteristics of the formed axial jets are further presented and discussed in comparison to jets that evolve in corresponding configurations with a single free surface.

II. EXPERIMENTAL METHODS

The test cell used in the experiments was fabricated by inserting an acrylic tube (7 mm external diameter and 1 mm wall thickness) at the bottom of a standard polystyrene cuvette with a 10 mm side (internal) and 45 mm height, as illustrated in Fig. 1. The tube was aligned collinear to the cuvette walls and secured at the bottom by applying silicone glue around the contact line to prevent the liquid from leaking out.

To attain a stable liquid layer, the cuvette was partially filled with de-ionized (DI) water, and then air was slowly injected through the tube using a syringe pump until a bubble formed at the output. It is crucial to introduce the gas into the cuvette gradually to prevent the bubble from detaching and floating to the free surface of the liquid. Consequently, the upper and lower gas–liquid interfaces encompass a thin layer of liquid whose thickness can be adjusted by varying the amount of water initially deposited inside the cuvette.

The laser-induced cavities are formed when the light beam emitted by a pulsed laser (Litron Nano T-250-10; $\lambda = 532$ nm; FHMW = 7 ns) is focused onto the liquid layer using a microscope objective (L Plan 10X/0.25) positioned over the top of the cuvette (see Fig. 1). The energy of the laser pulse was adjusted to approximately 10 mJ, leading to bubbles with a maximum radius $R_{\max} \sim 500 \mu\text{m}$.

The bubble jetting dynamics was captured using a high-speed camera *Photron SA-Z* equipped with a long-distance microscope *Mitutoyo 5X*. Using this setup, we captured video recordings at a rate of 210 000 frames per second (fps) acquired with an exposure time of 200 ns. The resolution of the imaging system was roughly $10 \mu\text{m}$ per pixel. The illumination was carried out with continuous white LED light reaching the camera lens from the observation direction (i.e., back-lighting). The experimental trials were conducted at a room temperature of around 25°C .

For the sake of direct comparison between experiments and simulations, the time and spatial dimensions of experimental bubbles are presented in their scaled forms according to Eq. (4), if not stated otherwise. The former is centered at $t_{\max, \text{exp}}^h$ —the occurrence of maximum characteristic horizontal length $R_{\max, \text{exp}}^h$, also horizontal “radius,” and is scaled according to the factor s . Here, subscripts “exp” and “sim” denote the values obtained from experiments and simulations. The same scaling is applied to spatial dimensions, whereas centering is performed by placing a coordinate system at the location of bubble formation

$$\begin{aligned} s &= \frac{R_{\max, \text{sim}}^h}{R_{\max, \text{exp}}^h} \\ R_{\text{exp}}^h &= s R_{\text{exp}}^h \\ t_{\text{exp}} &= s \left(t_{\text{exp}} - t_{\max, \text{exp}}^h \right) + t_{\max, \text{sim}}^h \end{aligned} \quad (4)$$

Both $R_{\max, \text{exp}}^h$ and the corresponding $t_{\max, \text{exp}}^h$ are determined through high-speed imaging, which, presently at 210 000 fps, yields roughly 20 images until the time of bubble collapse t_c . Presently, R_{\max}^h is more suitable than the equivalent radius R_{\max}^{eq} , as it can be conveniently measured from high-speed imaging when $D_1^* \text{ and } D_2^* \lesssim 1$. In the case of unbounded bubbles, the actual radii are considered, and thus, superscript h is omitted. The expected measurement error for bubble radii R and stand-off distances d is $10 \mu\text{m}$. For parameter D^* , this yields the expected error between 0.02 and 0.03.

III. NUMERICAL METHODS

Numerical simulations were performed to provide insight beyond the resolution of the experiment. We consider compressible, viscous, multiphase flow and employ a finite volume method-based solver *Ansys Fluent*⁴⁶ along with a volume of fluid method to capture the interface between phases. In the present case, three fluid phases are considered—vapor bubble, ambient gas, and ambient liquid. In Secs. III A–III G, quantities and properties specific to each phase are marked by a corresponding subscript $i = v, g, l$, which denotes the vapor, gas, and liquid phase, respectively. Their interface is assumed to remain sharp during the bubble lifetime and the presence of non-condensable gases inside the bubble is neglected.

A. Conservation laws

Equation of mass conservation for each phase can be written as

$$\frac{\partial(\alpha_i \rho_i)}{\partial t} + \nabla \cdot (\alpha_i \rho_i \mathbf{U}_i) = S_i \quad (5)$$

Here, ρ and \mathbf{U} denote the density and velocity vector field, respectively. Mass transfer in the form of phase change is considered through mass source terms S_i . Presently, the phase interface is captured by solving

continuity equation for the volume fraction fields of the gas ($i = g$) and liquid ($i = l$) phase. The volume fraction field α_v of the vapor phase can be obtained as

$$\alpha_v = 1 - \alpha_g - \alpha_l. \quad (6)$$

After volume fraction fields are known, we can determine the volume-averaged fluid properties ϕ throughout the computational domain as

$$\phi = \sum_i \alpha_i \phi_i, \quad i = v, g, l. \quad (7)$$

In the present case, this is true for density ρ , dynamic viscosity μ , and thermal conductivity λ . Based on the determined material properties, a single momentum [Eq. (8)] and energy [Eq. (10)] equation can be solved, which yields the shared velocity \mathbf{U} and temperature \mathbf{T} fields.

Conservation of momentum can be written as Eq. (8), where terms on the left side represent the effect of inertial forces due to local and convective acceleration, respectively. The right-hand side of the equation includes the effects of pressure, viscous, and body forces, respectively. The effects of surface tension are included as a body force \mathbf{b} acting at the vapor-liquid and gas-liquid interface.

$$\frac{\partial}{\partial t}(\rho \mathbf{U}) + \nabla \cdot (\rho \mathbf{U} \otimes \mathbf{U}) = -\nabla p + \nabla \cdot \boldsymbol{\tau} + \mathbf{b}. \quad (8)$$

Here, p denotes the pressure, \mathbf{b} denotes the body forces, and $\boldsymbol{\tau}$ denotes the viscous stress tensor that can be written for Newtonian fluids as

$$\boldsymbol{\tau} = \mu \left[(\nabla \mathbf{U} + (\nabla \mathbf{U})^T) - \frac{2}{3} (\nabla \cdot \mathbf{U}) \mathbf{I} \right], \quad (9)$$

where μ is dynamic viscosity and \mathbf{I} the unit tensor.

Energy balance is described by Eq. (10), which includes the effects of thermal conduction and heat transfer due to phase change.

$$\frac{\partial}{\partial t}(\rho E) + \nabla \cdot (\mathbf{U}(\rho E + p)) = \nabla \cdot (\lambda \nabla T) + Q. \quad (10)$$

Here, E and λ represent total specific energy and thermal conductivity, whereas Q denotes the energy transfer term due to phase change. The total specific energy is considered as a mass averaged variable

$$E = \frac{\sum_{i=v,g,l} \alpha_i \rho_i E_i}{\sum_{i=v,g,l} \alpha_i \rho_i}, \quad (11)$$

where the total specific energy of each phase E_i can be expressed by the i th phase internal energy e_i as

$$E_i = e_i + \frac{|\mathbf{U}|^2}{2}. \quad (12)$$

B. Equations of state

All three phases are considered as compressible and are described according to the Noble-Abel Stiffened-Gas (NASG) equation of state (EOS).⁴⁷ Vapor and liquid are considered as water, whereas ambient gas is considered as air.

$$\rho_i(p, T) = \left[\frac{(\gamma_i - 1)C_{vi}T}{p + P_{\infty i}} + b_i \right]^{-1}, \quad (13)$$

$$e_i(p, T) = \frac{p + \gamma_i P_{\infty i}}{p + P_{\infty i}} C_{vi}T + q_i, \quad (14)$$

$$h_i(p, T) = \gamma_i C_{vi}T + b_i p + q_i, \quad (15)$$

$$c_i(p, \rho_i) = \sqrt{\frac{\gamma_i(p + P_{\infty i})}{\rho_i(1 - b_i \rho_i)}}. \quad (16)$$

Here, h and c denote enthalpy and sound speed, whereas γ , C_v , P_{∞} , b , and q are the material parameters. Depending on the selection of material parameters, the NASG EOS can be reverted either to the ideal gas ($P_{\infty} = 0$ and $b = 0$) or the stiffened gas equation of state. The former is presently true for vapor and gas phase ($i = v, g$). Additionally, a generalized form of the equation of state is employed, which also allows for the consideration of calorically imperfect gases.⁴⁸

$$\rho_i(p, T) = \frac{p}{R_i^* T}, \quad (17)$$

$$e_i(T) = e_{ref i} + \int_{T_{ref}}^T C_{vi} dT, \quad (18)$$

$$h_i(T) = h_{ref i} + \int_{T_{ref}}^T C_{pi} dT, \quad (19)$$

$$c_i(T) = \sqrt{\gamma_i R_i^* T}. \quad (20)$$

Here, R^* and C_p correspond to the specific gas constant and specific heat at constant pressure. The subscript “ref” refers to the value at the reference point (p_{ref} , T_{ref}). The considered values of material properties for all phases are given in the Appendix.

C. Phase change model

Mass transfer in the form of condensation between the liquid and vapor phase is considered according to the Lee’s model⁴⁹ as

$$S_v = -S_l = -r_{vl} \alpha_v \rho_v \frac{T_{sat} - T}{T_{sat}}, \quad \text{when } T < T_{sat}(p). \quad (21)$$

Here, r_{vl} is an empirical coefficient of mass transfer intensity that corresponds to condensation. The term T_{sat} denotes saturation temperature and is presently considered as a function of pressure $T_{sat} = T_{sat}(p)$. The corresponding energy transfer term Q in the energy equation is defined as

$$Q = (h_v - h_l) S_l, \quad (22)$$

where the difference between phase enthalpies, h_v and h_l , can be understood as latent heat of vaporization.

Phase change is included to account for a gradual mass loss of the vapor bubble, which significantly affects the bubble collapse and rebound intensity. This is especially prominent in laser-induced bubbles, which can lose more than 90% of their mass during the first collapse.⁵⁰ In the absence of condensation modeling or any other intervention that indirectly accounts for the gradual loss of bubble mass, e.g., equilibrium bubble radius correction,⁵¹ an initially pressurized bubble (see Sec. III G) will yield a weak bubble collapse and large rebounds, which is not characteristic of the presently considered laser-induced bubbles (see Sec. IV A).

The finally employed value for the condensation intensity factor $r_{vl} = 4.85 \times 10^7 \text{ s}^{-1}$ was determined based on the obtained

experimental results and data from previous research (see Sec. IV A). One of the downsides of the Lee's model is that the condensation intensity parameter is not necessarily independent of the chosen spatial resolution, as it depends on the gradient of the volume fraction fields at the phase interface. Thus, the value was adapted for convergence analysis on spherical bubbles in Sec. IV A according to the considered mesh resolution Δx and the bubble-liquid interface thickness (initialized as $2\Delta x$):

$$r_{vl}(\Delta x) = \frac{1.25 \times 10^{-6} \text{ m}}{\Delta x} 4.85 \times 10^7 \text{ s}^{-1}. \quad (23)$$

Data for saturation temperature and pressure are taken from the National Institute of Standards and Technology (NIST) database.⁵²

D. Surface tension model

The effects of surface tension at the vapor-liquid and gas-liquid interface are considered through a body force term \mathbf{b} in the momentum equation, according to the Continuum surface stress model:⁵³

$$\mathbf{b} = \nabla \cdot \mathbf{T}, \quad (24)$$

where \mathbf{T} is a surface stress tensor defined as

$$\mathbf{T} = \sigma_l(\mathbf{I} - \mathbf{n} \otimes \mathbf{n})|\nabla\alpha_l|. \quad (25)$$

Here, σ_l denotes the surface tension, and \mathbf{n} denotes the bubble surface and free surface normal. The latter is obtained as

$$\mathbf{n} = \frac{\nabla\alpha_l}{|\nabla\alpha_l|}. \quad (26)$$

E. Numerical details

For all calculations, the PISO pressure-velocity coupling algorithm⁵⁴ was employed, along with a first-order implicit temporal discretization. Regarding the spatial discretization, we used the pressure staggering option (PRESTO!) scheme⁵⁵ for pressure interpolation and the second-order upwind scheme for density, momentum, and energy interpolation. Phase interfaces were captured using a Piecewise linear interface calculation (PLIC) geometric reconstruction scheme,⁵⁶ which assumes that the interface between two fluids has a linear slope within each computational cell.

F. Mesh and time step

All cases were evaluated under the assumption of axial symmetry on a rectangular domain spanning $200R_{\max}$ from the bubble center. Temporal and spatial resolution were chosen based on the convergence analysis (see Sec. IV A) and available computational resources. Orthogonal mesh with constant resolution of $\Delta x = 1.25 \mu\text{m}$ in the region of the bubble and the water-air interface was used. Cells are gradually coarsened with the distance toward the domain's edge. Time step was determined by the Courant-Friedrichs-Lewy condition of $\frac{\Delta t}{\Delta x}(u_x + u_y) \leq C_{\max} = 0.2$, where u_x and u_y denote the magnitudes of the velocity in the radial and axial direction, respectively. Additionally, a low time step increase factor $\delta t = 1.0015$ is considered to retain the acoustic Courant number below unity until shock waves propagate beyond $\sim R_{\max}$ from the bubble center.

G. Initial and boundary conditions

Boundary conditions at the end of the computational domain were set to wave nonreflecting pressure outlet with $p_\infty = 10^5 \text{ Pa}$ and $T_\infty = 25 \text{ }^\circ\text{C}$. We assume an initially spherical bubble with radius $R_0 = 25 \mu\text{m}$ in ambient fluid at rest and even pressure and temperature fields of p_∞ and T_∞ . The initial bubble radius was chosen based on the size of the vertical semiaxis of the experimentally obtained ellipsoidal plasma spots. The rate and extent of bubble expansion and collapse is controlled by two parameters: the initial equilibrium radius R_{eq0} and condensation intensity factor r_{vl} . The values of both parameters were found through a trial-and-error approach, such that the results were concordant with the obtained experimental data and previous research on unbounded bubbles (see Sec. IV A). Instantaneous equilibrium bubble radius R_{eq} is directly related to its instantaneous mass and represents a fictitious radius that an unbounded bubble would eventually attain given a set of boundary conditions (p_∞ and T_∞) and under isentropic conditions. The internal bubble equilibrium pressure and temperature are $p_{eq} = p_\infty + \frac{2\sigma}{R_{eq}}$ and $T_{eq} = T_\infty$. First, the value of $r_{vl} = 4.85 \times 10^7 \text{ s}^{-1}$ was found through simulations of bubble collapse from the maximum bubble size onward [$R_{\max} = 500 \mu\text{m}$, $T_0 = T_\infty$, and $p_0 = p_{sat}(T_0)$], until the desired collapse and rebound intensities were obtained. Second, the value of equilibrium radius of $R_{eq0} = 209 \mu\text{m}$ was obtained for the case of an initially expanding bubble, which yields the initial bubble mass $m_0 = 2.81 \times 10^{-11} \text{ kg}$ and along with an assumption of an isentropic process determines the initial bubble pressure p_0 and temperature T_0 .

IV. RESULTS AND DISCUSSION

A. Model validation and convergence analysis for unbounded bubbles

Both model validation and convergence analysis were initially performed for the case of an unbounded laser-induced bubble. Shown in Fig. 2 are the experimental results (blue dots) for unbounded bubbles that attain $R_{\max*} = 544 \pm 75 \mu\text{m}$ (mean \pm SD, $N = 7$). The time and instantaneous radii of experimental bubbles are presented in their centered and scaled forms, as described in Sec. II. The numerical simulation (black line, $R_{\max} = 500 \mu\text{m}$, $t_{\max} = 46.9 \mu\text{s}$, and $t_c = 93.9 \mu\text{s}$) with spatial resolution $\Delta x = 1.25 \mu\text{m}$ shows very good agreement with experimental results until the second bubble collapse. The same

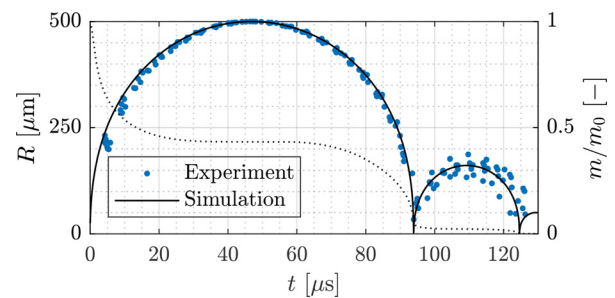


FIG. 2. Numerical model validation for the case of an unbounded bubble. Numerical simulation ($R_{\max} = 500 \mu\text{m}$, $t_{\max} = 46.9 \mu\text{s}$, and $t_c = 93.9 \mu\text{s}$) shows a very good agreement with experimental results ($R_{\max*} = 544 \pm 75 \mu\text{m}$, $N = 7$) until the second bubble collapse. Experimental results are scaled as described in Sec. II. Dotted line denotes the instantaneous bubble mass ratio m/m_0 from the numerical simulation, where initial mass is $m_0 = 2.81 \times 10^{-11} \text{ kg}$.

TABLE I. Convergence analysis for the case of an unbounded laser-induced bubble. All cases were computed with the time step condition of $C_{\max} = 0.2$. Resolution-independent solutions are given in the bottom row and were estimated according to the Richardson extrapolation.

Δx (μm)	δt (-)	N_{cells} (10^6)	R_{max} (μm)	R_{min} (μm)	R_{reb} (μm)	$ \frac{dR}{dt} _{\text{max}}$ (km/s)
2.50	1.0030	0.30	499	3.24	157	1.38
1.77	1.0021	0.60	500	2.96	160	1.48
1.25	1.0015	1.21	500	2.81	161	1.54
$1/\infty$	1	∞	501	2.65	166	1.66

resolution was also chosen for all further simulations based on the results of a convergence analysis presented below and the available computational resources.

The results of the convergence analysis are gathered in Table I, where R_{max} , R_{min} , and R_{reb} are the maximum, minimum, and rebound radius, whereas $|\frac{dR}{dt}|_{\text{max}}$ denotes the peak collapse velocity. The convergence analysis shows that the rebound radius begins to converge only after the mesh resolution becomes finer than the estimated collapse radius, e.g., at $\Delta x = 5 \mu\text{m}$, we obtain $R_{\text{reb}} = 164 \mu\text{m}$. This also imposes a relatively fine resolution as we consider strongly collapsing bubbles with $\frac{R_{\text{max}}}{R_{\text{min}}} \sim 200$. Strong collapses are also evident from the obtained supersonic peak collapse velocities with regard to water at ambient conditions. Presently, the characteristic bubble expansion and collapse velocities are $\frac{R_{\text{max}} - R_0}{t_{\text{max}}} = 10.1 \text{ m/s}$ and $\frac{R_{\text{min}} - R_{\text{max}}}{t_c} = -10.6 \text{ m/s}$, respectively. Peak collapse pressure and temperature, obtained as volume averages in the vapor phase at the first bubble collapse, amount to 18.6 GPa and 2.65 kK, respectively. However, we do acknowledge that both parameters unsurprisingly exhibit slower rates of convergence with the estimated errors on the order of a few tens of percent at $\Delta x = 1.25 \mu\text{m}$. The same is true for the shock wave magnitude at R_{max} from the bubble center, which is obtained to be 19.5 MPa at the finest resolution considered. For reference, considering a simplified case of adiabatic compression, the bubble collapse pressure is $\propto R_{\text{min}}^{-3\gamma}$, which for a vapor bubble ($\gamma = \frac{4}{3}$) with an estimated error in R_{min} of 6% yields a bubble collapse pressure error of -21% .

B. Bubble dynamics and jetting regimes in a thin liquid layer at null Kelvin impulse

Here we focus on varying single bubble dynamics and jetting regimes in a strongly confined environment at null Kelvin Impulse. This implies a symmetric bubble environment, which presently consists of two opposite flat free surfaces (air-water interface). We consider standoff parameter pairs of $D^* = 1, 0.7, 0.4, 0.25,$ and 0.15 . These are selected based on previous research²³ on bubble dynamics near a single free surface and in that case correspond to highly anisotropic environments, where the formation of strong jets is expected.²⁷ One can observe that experimental water-air interfaces are not exactly flat, which is especially evident for the bottom “free” surface. The reasons behind this are physical constraints of the utilized experimental setup, described in Sec. II. We do acknowledge that surface curvature can significantly affect the propagation of bubble-emitted shock waves and the resulting phenomena. On the other hand, we do not expect any major influences on the overall bubble dynamics, since the curvature

radii of free surfaces are significantly larger than both characteristic length scales—maximum bubble radius R_{max} and bubble-interface stand-off distance d .

The results are presented as image sequences and accompanying videos for both experimental and simulated bubbles. The latter allows for a more detailed insight into the phenomenon, out of the reach of the presently employed experimental methods, whereas the former primarily serves as a means of validating the numerical methodology and the obtained results. The primary focus is given to bubble shape progression, characteristics of the resulting jets, counter-jets, and the development of interfacial instabilities.

The overall agreement between experimental and numerical results is very good until the first bubble collapse. Later, during the rebound the quantitative differences arise and gradually accumulate, while the overall qualitative agreement is preserved. Presently, the main focus lies in the bubble dynamics and accompanying phenomena in their primary growth-collapse cycle, included in attached image sequences. Interested readers are referred to the accompanying video files, which include the evolution of experimental bubbles throughout their whole lifetime.

1. Broad jets ($D^* = 1$)

Figure 3 shows sequences of experimental [Fig. 3(a), Multimedia view] and simulated [Fig. 3(b), Multimedia view] bubbles initialized at $d = 500 \mu\text{m}$ from both free surfaces ($D^* = 1$). During the initial phase of expansion, the bubble retains its spherical shape, gradually deforming into an ellipsoidal shape with the major axis along the axis of symmetry. The aspect ratio continually changes throughout its lifetime, hinting at a separate oscillation frequency in each of the two major directions: axial (vertical) and radial (horizontal). The maximum bubble volume is reached at $34.7 \mu\text{s}$ with $R_{\text{max}}^{\text{eq}} = 529 \mu\text{m}$, and the characteristic rate of bubble expansion of 14.5 m/s exceeds that of an unbounded bubble by roughly 43%. At that time, the bubble already begins to contract vertically ($R_{\text{max}}^{\text{v}} = 581 \mu\text{m}$); however, this is not yet the case for the horizontal direction ($R_{\text{max}}^{\text{h}} = 505 \mu\text{m}$).

Only well into the contraction phase, after $43 \mu\text{s}$ from bubble inception, both poles invert into uniaxial jets, forming a concave bubble shape. The jets closely resemble the shape of a standard uniaxial jet that is formed when a bubble evolves in other moderately anisotropic environments, e.g., near a rigid surface. The mean jet speed amounts to 21.9 m/s ; however, both jets continue to accelerate toward each other and reach the peak speed of 27.5 m/s . With characteristic jet radius r_{jet} of $101 \mu\text{m}$, the corresponding Reynolds and Weber numbers amount to 6210 and 2110. These are defined as $\text{Re}_{\text{jet}} = 2\rho_l v_{\text{jet}} r_{\text{jet}} / \mu_l$ and $\text{We}_{\text{jet}} = 2\rho_l v_{\text{jet}}^2 r_{\text{jet}} / \sigma_l$, respectively, where v_{jet} denotes the characteristic jet speed.

The jet impact at $t = 66.8 \mu\text{s}$ [Fig. 4(a)] leads to peak impact pressure of 243 bars and emission of a weak pressure wave that propagates outward, along the axis of symmetry. The bubble assumes a toroidal shape with a sharp circular edge toward its center, formed because of the impact of two opposing jets with curved heads. The ongoing impact of the progressively wider jet heads causes the outward movement of the circular edge, which is accelerated to almost 650 m/s . The jet impact corresponds to a closing gap, eventually leading to the ejection of water in the form of a sheet. As a result, the initially focused water flow along the axis of symmetry is redirected outward in the

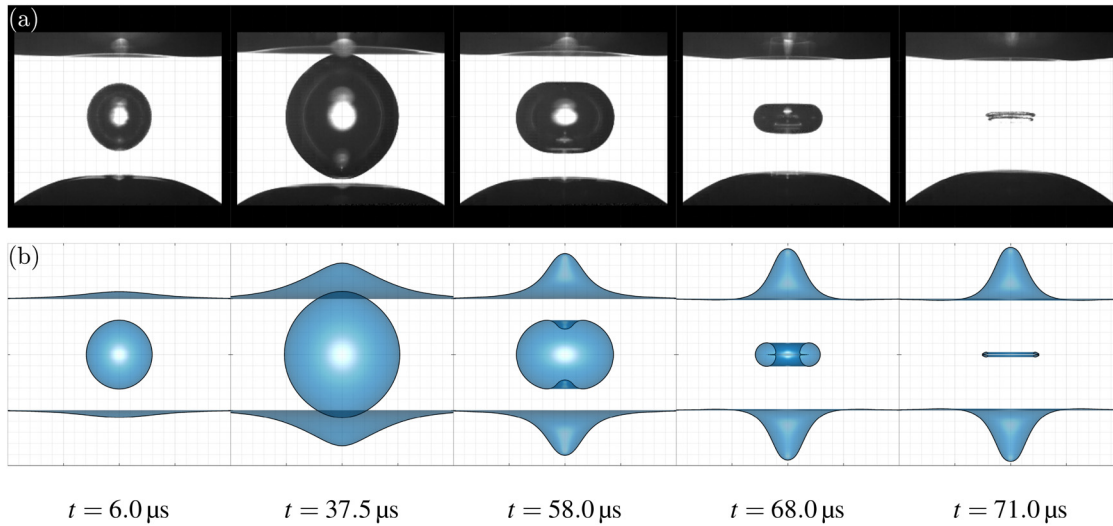


FIG. 3. Image sequence representing the broad jet regime ($D^* = 1$): $R_{\max}^h = 518 \mu\text{m}$, $t_{\max}^h = 37.3 \mu\text{s}$, and $\Delta t_{\text{exp}} = \pm 1.73 \mu\text{s}$. (a) Experimental bubble ($R_{\max, \text{exp}}^h = 711 \mu\text{m}$) and (b) simulated bubble: during initial expansion ($t = 6.0 \mu\text{s}$); around maximum horizontal expansion ($t = 37.5 \mu\text{s}$); after formation of opposing uniaxial jets ($t = 58.0 \mu\text{s}$); after jet impact, during annular outflow ($t = 68.0 \mu\text{s}$); and immediately after the collapse, when a vertically stacked torus pair reemerges ($t = 71.0 \mu\text{s}$). Width and height of each subfigure correspond to 2 mm. Minor grid spacing is $100 \mu\text{m}$. Numerical sequence shows volume fraction isosurfaces at $\alpha = 0.5$. Multimedia available online.

radial (horizontal) direction, causing the shape inversion of the circular edge.

The resulting annular outflow spreads along the central horizontal plane ($y = 0$) in a very thin layer ($\text{Re}_{\text{tip}} = 240$ and $\text{We}_{\text{tip}} = 320$),

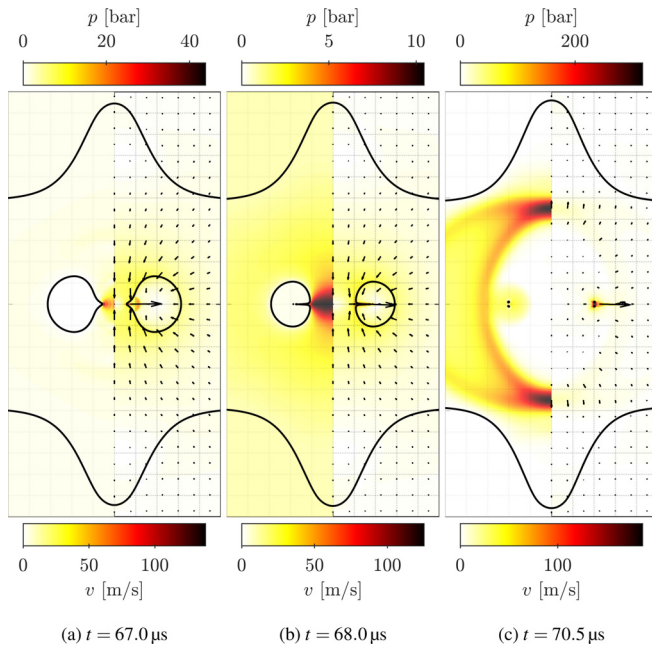


FIG. 4. Details behind (a) the impact of opposing broad jets ($D^* = 1$); (b) the resulting annular outflow; and (c) collapse of the remaining vertically stacked toroidal bubble pair. Shown are pressure (left) and velocity (right) contours. Phase interfaces are drawn with a solid black line. Width and height of each subfigure corresponds to 1 and 2 mm, respectively. Grid spacing is $100 \mu\text{m}$.

with the tip thickness of $h_{\text{tip}} \approx 2 \mu\text{m}$ [Fig. 4(b)]. The propagation speed of the annular outflow is significantly faster than that of the preceding axial jets. Between its formation ($67 \mu\text{s}$) and bubble piercing ($69 \mu\text{s}$), the tip travels $215 \mu\text{m}$, which yields the mean speed of 108 m/s . Almost instantly after annular outflow formation, its tip is destabilized by the Plateau–Rayleigh instability and breaks into smaller outwardly directed droplets (Fig. 5). Based on the dimensional analysis,⁵⁷ the critical time and length scales for its onset are approximated as $t_{\text{crit}} \sim (\rho_l h_{\text{tip}}^3 / \sigma)^{1/2} \approx 0.3 \mu\text{s}$ and $L_{\text{crit}} \sim v_{\text{tip}} t_{\text{crit}} \approx 35 \mu\text{m}$, which aligns with the obtained numerical results.

The outflow eventually pierces the bubble from within and reemerges at the equator, which leads to the splitting of a toroidal bubble into two symmetric counterparts. The ejected vaporous volume, however, breaks down and condenses into the liquid. The remaining vertically stacked toroidal bubble pair continues to contract and attracts a flow that converges toward the circular centroids of the remaining toruses in the horizontal plane. Their collapse ($t = 70.2 \mu\text{s}$) yields an emitted shock wave that converges at the axis of symmetry and reaches the magnitude of several hundred bar [Fig. 4(c)]. The collapse can be

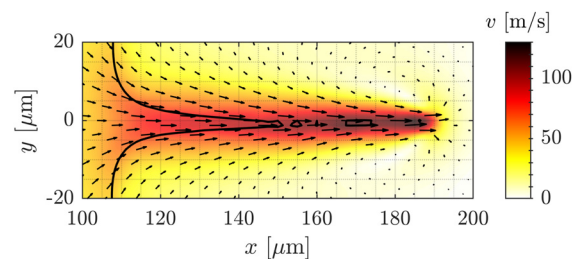


FIG. 5. The onset of the Plateau–Rayleigh instability causes the breakup of the water sheet tip. The numerical bubble shape (black solid line, $\alpha_v = 0.5$) and velocity field contours are shown at $t = 68 \mu\text{s}$.

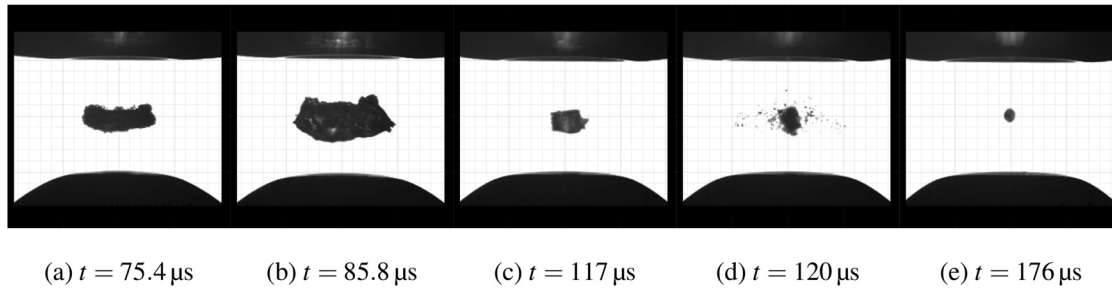


FIG. 6. Experimental image sequence representing the broad jet regime ($D^* = 1$) after the first bubble collapse: (a) formation of a single torus with irregularly shaped boundaries, (b) the primary bubble expansion during the rebound is directed in the horizontal direction, (c) the second implosion is oriented along a sink-type flow toward a center point, (d) a cloud of secondary cavitation is formed after the second bubble collapse, and (e) bubble during the fifth contraction cycle exhibits a net zero vertical displacement. Width and height of each subfigure correspond to 2 mm. Minor grid spacing is $100 \mu\text{m}$.

characterized as strong; however, the pressure and temperature peaks of 0.32 GPa and 1100 K are significantly reduced in comparison to an equivalent unbounded bubble with 18.6 GPa and 2650 K, respectively (see Sec. IV A).

After the first bubble collapse, a vertically stacked torus pair reemerges (Fig. 3 at $t = 71.0 \mu\text{s}$) and the annular outflow continues to dictate the bubble shape. The following bubble shape progression is included in Fig. 6 and also as multimedia to Fig. 3(a). As the torus pair expands, it eventually merges into unity, forming a single torus with irregularly shaped boundaries [Fig. 6(a)]. The primary expansion during the rebound is directed in the horizontal direction, and the bubble almost reattains its maximum horizontal dimension [Fig. 6(b)]. Protrusion of annular outflow at the equator is evident until the bubble is well in the second stage of contraction. The implosion is oriented along a sink-type flow toward a center point, which results in a major bubble contraction in the horizontal direction [Fig. 6(c)]. After the second collapse, a cloud of secondary cavitation is also evident, spanning approximately the volume previously occupied by the rebounding bubble [Fig. 6(d)]. Interestingly, in the present geometrical configuration, secondary cavitation is observed only at the second collapse and is not evident at the first collapse or any other subsequent events in which the bubble undergoes progressively less violent volume oscillations with its shape alternating between both major directions. Eventually, the bubble contents diffuse and condense into the surrounding liquid. Overall, the bubble volume does not undergo any net vertical displacement [Fig. 6(e)], which is to be expected due to a symmetric nature of a null Kelvin impulse environment.

Already at $D^* = 1$, the free surfaces undergo large deformations induced by the expanding bubbles, such that a thick layer of water remains to clearly divide the bubble contents and the ambient air. With the formation of opposing broad jets and bubble contraction, both free surfaces continue to deform and shape counter jets. A characteristic crown-shaped perturbation²³ of free surfaces forms and grows only after the bubble collapses and undergoes a second stage of expansion.

2. Mushroom-capped jets ($D^* = 0.7$)

Image sequences of an experimental and simulated bubble initialized at $d = 350 \mu\text{m}$ from both free surfaces ($D^* = 0.7$) are shown in

Fig. 7(a) (Multimedia view) and Fig. 7(b) (Multimedia view), respectively. Overall, the bubble expansion is qualitatively similar to the broad jet regime ($D^* = 1$, see Sec. IV B 1). With smaller D^* , the bubble shape exhibits a higher aspect ratio and resembles an egg shape at maximum expansion (Fig. 7 at $t = 18.5 \mu\text{s}$). With $R_{\text{max}}^v = 659 \mu\text{m}$, the vertical expansion reaches almost double the initial standoff distance from the free surfaces. This is shortly followed by the inversion of both poles, marking the beginning of jet formation at $27.5 \mu\text{s}$, which occurs even before the bubble expands to its maximum volume ($R_{\text{max}}^{\text{eq}} = 525 \mu\text{m}$) at $28.9 \mu\text{s}$. Although the maximum bubble volume is similar to the broad jet case ($D^* = 1$), the characteristic bubble expansion rate of 17.3 m/s hints toward a progressively more explosive bubble expansion with smaller D^* . At $33.5 \mu\text{s}$, when $R_{\text{max}}^h = 505 \mu\text{m}$ is reached, the opposing jets can already be clearly seen concealed within the numerical bubble; however, the mushroom-shaped caps develop only later, when both jets continue to accelerate toward the bubble center and reach the peak speed of 34.0 m/s, with the mean jet speed of 26.8 m/s.

Jet impact at $t = 51.9 \mu\text{s}$ [Fig. 8(a)] leads to a peak impact pressure of 389 bars and emission of a weak pressure wave. As mushroom-shaped jet caps meet at the horizontal plane ($y = 0$), a sharp circular edge is formed and accelerated beyond 1000 m/s, showing qualitative similarity to the broad jet case (see Fig. 4). Also here, a sharp inwardly oriented edge is inverted along the radial direction, which prevents its entrapment by the remaining axial flow. Jet impact leads to the formation of a toroidal bubble, clearly seen also from high-speed imaging [Fig. 7(a) at $t = 54.5 \mu\text{s}$].

A stronger jet impact than in the broad jet case results in even thinner and faster annular outflow, with the tip thickness of $1.4 \mu\text{m}$, which is almost instantly ($t_{\text{crit}} \approx 0.2 \mu\text{s}$) destabilized and atomized [Fig. 8(b)]. While the torus continues to contract, the resulting droplets pierce the bubble from within and erupt at the equator. The annular outflow is progressively thickened as both necks of uniaxial jets are redirected in the radial direction. Before collapsing, the bubble is further split into two opposing toruses. This is similar to the broad jet case; however, the remaining bubble volume is larger as it happens in an earlier stage of the collapse. Smaller bubble volumes erupt at the equator along with the annular outflow; however, they collapse and condense separately and before the main bubble. The remaining vertically stacked toruses further break down and sequentially collapse

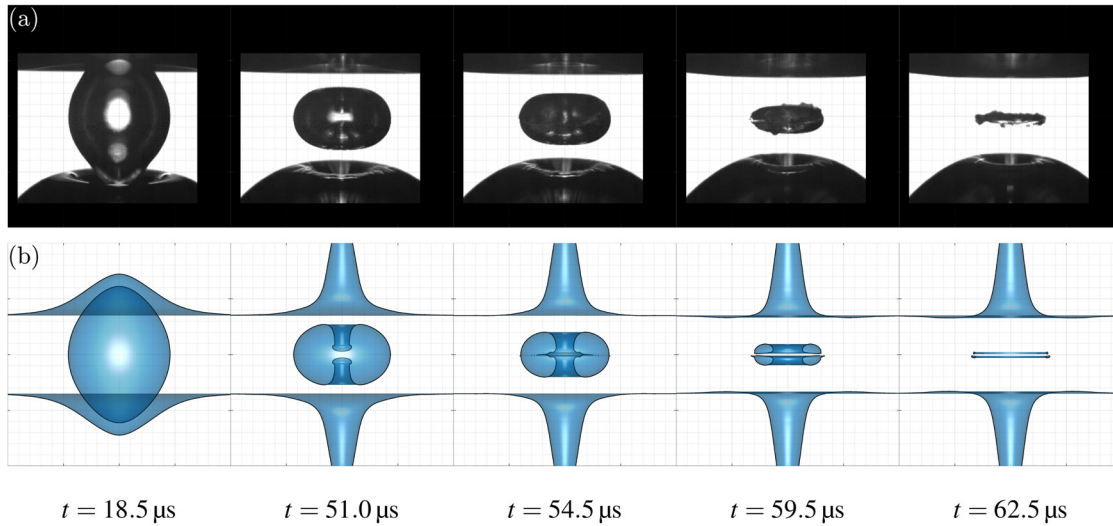


FIG. 7. Image sequence representing the mushroom-capped jet regime ($D^* = 0.7$): $R_{\max}^h = 505 \mu\text{m}$, $t_{\max}^h = 33.5 \mu\text{s}$, and $\Delta t_{\text{exp}} = \pm 1.50 \mu\text{s}$. (a) Experimental bubble ($R_{\max, \text{exp}}^h = 803 \mu\text{m}$) and (b) simulated bubble: during expansion into an egg-like shape ($t = 18.5 \mu\text{s}$); after the opposing axial jets develop mushroom-capped fronts ($t = 51.0 \mu\text{s}$); when a toroidal bubble is formed after the jets impact ($t = 54.5 \mu\text{s}$); after radial outflow further splits the bubble into two opposing toruses ($t = 59.5 \mu\text{s}$); and immediately after the collapse, when a double torus is formed again during the initial phase of the rebound ($t = 62.5 \mu\text{s}$). Width and height of each subfigure correspond to 2 mm. Minor grid spacing is $100 \mu\text{m}$. Numerical sequence shows volume fraction isosurfaces at $\alpha = 0.5$. Multimedia available online.

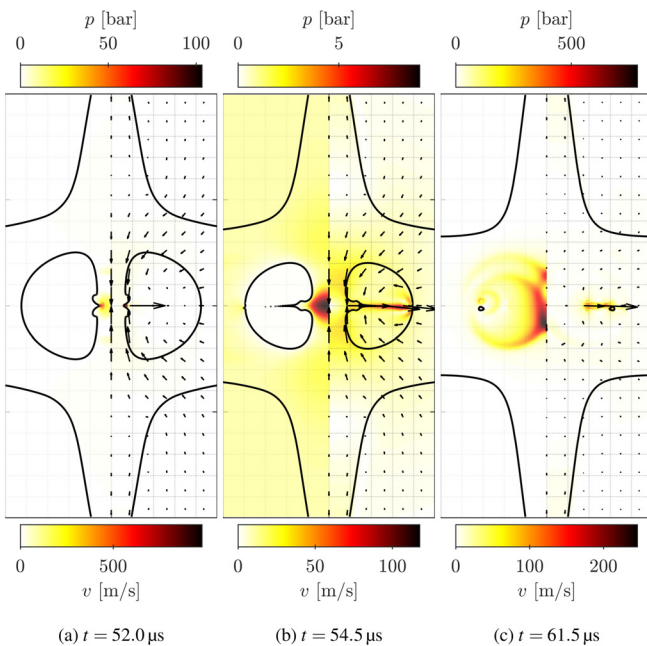


FIG. 8. Details behind (a) the impact of opposing mushroom-capped jets ($D^* = 0.7$); (b) the resulting annular outflow; and (c) collapse of the remaining vertically stacked toroidal bubble pair. Shown are pressure (left) and velocity (right) contours. Phase interfaces are drawn with a solid black line. Width and height of each subfigure corresponds to 1 and 2 mm, respectively. Grid spacing is $100 \mu\text{m}$.

between 61.3 and 61.7 μs , which yields the strongest characteristic bubble contraction velocity, -15.8 m/s , of all cases considered. Similar can also be said for multiple shock waves that are emitted and converge at the axis of symmetry with a magnitude of almost 1000 bars [Fig. 8(c)].

The bubble shape progression after the first collapse is included in Fig. 9 and also as multimedia to Fig. 7(a). During the bubble rebound, at 70 μs , the crown is formed; however, the primary counterjets have already protruded 1.5 mm into the ambient air. The dynamics of a rebounding bubble is qualitatively very similar to the broad jet scenario ($D^* = 1$). Here, the horizontal dimension attained during the rebound actually surpasses R_{\max}^h [Fig. 9(a)]. This can be partially attributed to a higher momentum attained by the mushroom-capped jets, leading to a stronger annular outflow. However, another reason is also a larger rebound volume than in the broad jet case. This implies a less intense first collapse, which might seem discordant with the strongest mean bubble collapse rate mentioned previously. Nevertheless, a less intense first collapse is also evident from simulations when comparing the minimal bubble volumes attained along with pressure and temperature peaks.

Secondary cavitation is observed after the second [Fig. 9(b)] and third [Fig. 9(c)] collapses. However, it can also be observed immediately after the bubble creation along the axis of symmetry, near both free surfaces. This results from the passage of a Prandtl–Meyer tension wave reflected from both free surfaces.³⁸ Numerical simulations did not capture this phenomenon, as we have decided to only account for condensation in Lee’s model (see Sec. III). Conceptually, the model should also be able to at least qualitatively capture secondary cavitation with the inclusion of an appropriate evaporation coefficient $r_{h,}$ as its

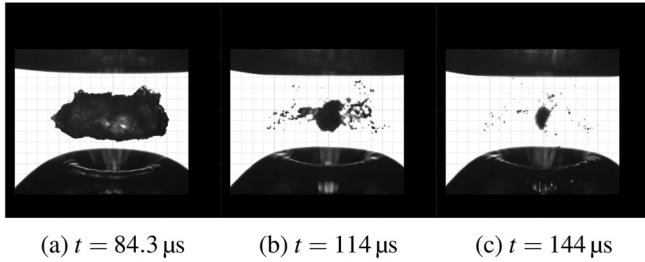


FIG. 9. Experimental image sequence representing the mushroom-capped jet regime ($D^* = 0.7$) after the first bubble collapse: (a) maximum horizontal bubble dimension during the rebound surpasses R_{\max}^h , and the onset of secondary cavitation after the (b) second and (c) third bubble collapse. Width and height of each subfigure correspond to 2 mm. Minor grid spacing is $100 \mu\text{m}$.

formulation does not require an existing phase interface to account for phase change. However, based on our current work, we find the selection of a single constant parameter r_{lv} as difficult, if not inappropriate. Presently, it also dictates the mass transfer between the ambient liquid and the bubble, a fundamentally different phenomenon, which is not likely to conform to the same-valued empirical coefficient r_{lv} .

3. Cylindrical jets ($D^* = 0.4$)

A bubble initiated $200 \mu\text{m}$ from both free surfaces ($D^* = 0.4$) explosively expands into an elongated shape that protrudes into the free surfaces beyond four times ($R_{\max}^v = 828 \mu\text{m}$) the initial standoff distance [see Fig. 10(a) (Multimedia view) and Fig. 10(b) (Multimedia view)]. The characteristic expansion rate is 2.5 times that of an unbounded bubble, amounting to 25.1 m/s . However, despite the vigorous expansion, a thin liquid layer between the bubble and ambient

air remains stable and unbroken. Both poles invert their shape toward the center at $13 \mu\text{s}$, while the bubble is still expanding in all directions.

The maximum volume ($R_{\max}^{\text{eq}} = 493 \mu\text{m}$) in the present case is now reduced compared to the unbounded case ($R_{\max}^{\text{eq}} = 500 \mu\text{m}$), which suggests a cushioning effect when bubbles evolve in highly bounded environments. At that time, $t = 18.6 \mu\text{s}$, both jets are already clearly formed with thin necks (radius $\sim 20 \mu\text{m}$) and mushroom-shaped caps [Fig. 11(a)]. While the presently employed backlight illumination prevented us from observing this phenomenon experimentally, it is clearly depicted in previous experimental work [see penultimate image in Fig. 12(e) by Rosselló *et al.*,²³ which corresponds to $D^* = 0.38$]. Nevertheless, the developed mushroom caps are unstable and break up due to the onset of Rayleigh–Taylor instability [Fig. 11(b)], which causes jet tips to become hemispherical by $26.3 \mu\text{s}$ (Fig. 10 at $t = 26.5 \mu\text{s}$), when the bubble reaches $R_{\max}^h = 461 \mu\text{m}$. At that time, remnants of instabilities can still be seen as minor shape irregularities in the form of small droplets reattached to the necks of both jets as they accelerate toward each other. With 51.0 and 77.7 m/s , both the mean and maximum jet speeds practically double in magnitude when D^* is reduced from 0.7 (mushroom-capped jets) to 0.4 (cylindrical jets). The same is also true for the peak impact pressures, which reach 700 bars .

Following the jet impact [$t = 28.7 \mu\text{s}$, see Fig. 12(a)], the resulting flow is redirected in the radial direction, similar to the mushroom-capped jet case ($D^* = 0.7$, see Sec. IV B 2). Here as well, the circular edge momentarily exceeds the speed of 1000 m/s before its shape inverts and the tip fragments into droplets [Figs. 12(a) and 12(b)]. In addition to tip breakdown, the annular outflow presently also develops a flapping shape instability, which can be observed inside the simulated bubble in Figs. 10(b) ($t = 32.0 \mu\text{s}$) and 12(b). This phenomenon, also known as the flapping regime, is further discussed in Sec. IV C and has already been well documented for liquid sheets produced when the

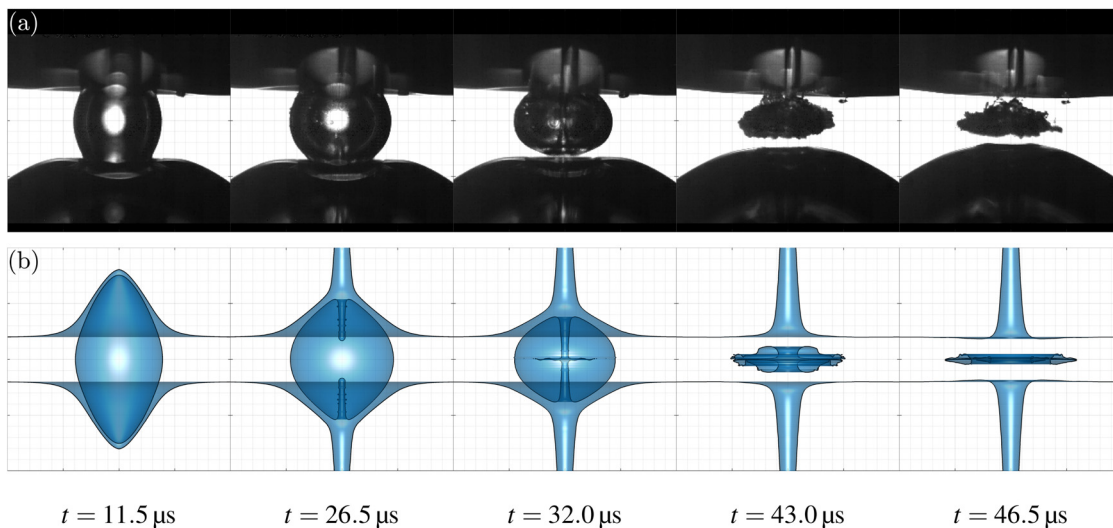


FIG. 10. Image sequence representing the cylindrical jet regime ($D^* = 0.4$): $R_{\max}^h = 461 \mu\text{m}$, $t_{\max}^h = 26.3 \mu\text{s}$, and $\Delta t_{\text{exp}} = \pm 1.83 \mu\text{s}$. (a) Experimental bubble ($R_{\max, \text{exp}}^h = 599 \mu\text{m}$) and (b) simulated bubble: during expansion into an elongated shape ($t = 11.5 \mu\text{s}$); after jets attain a cylindrical shape ($t = 26.5 \mu\text{s}$); when the water sheet succeeding the jet impact exhibits a shape instability ($t = 32.0 \mu\text{s}$); during toroidal bubble contraction and formation of irregularly shaped outer rim ($t = 43.0 \mu\text{s}$); and after the bubble shape is split into two parts and just before collapse of the main (inner) vapor volume ($t = 46.5 \mu\text{s}$). Width and height of each subfigure correspond to 2 mm. Minor grid spacing is $100 \mu\text{m}$. Numerical sequence shows volume fraction isosurfaces at $\alpha = 0.5$. Multimedia available online.

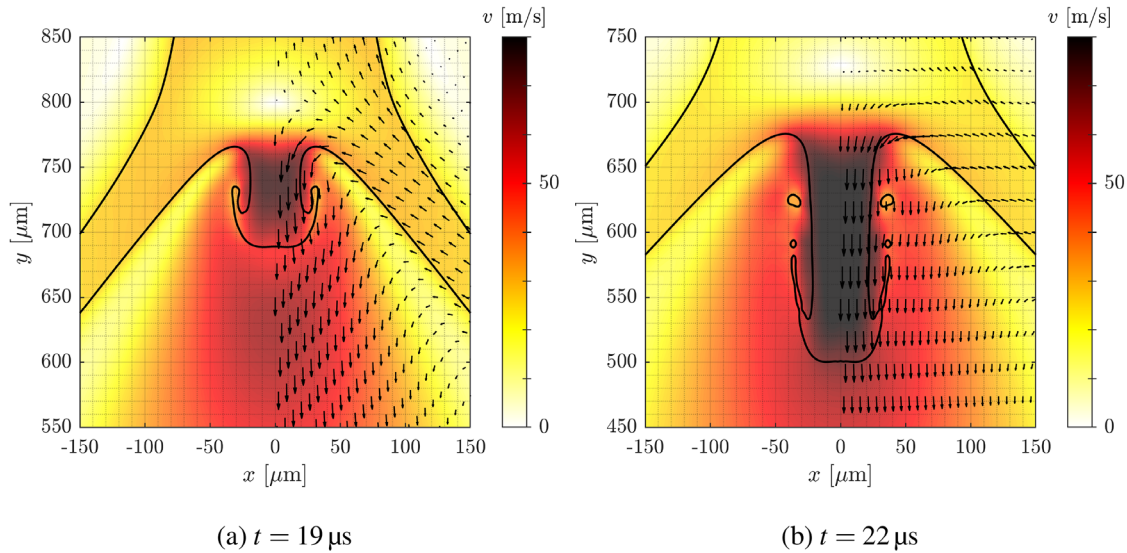


FIG. 11. Cylindrical jets form (a) unstable mushroom-shaped caps and (b) which undergo breakdown, resulting in the rounding of the jet tip. Shown are phase interfaces (black solid line, $\alpha = 0.5$) and velocity field contours.

ejection angle of a water jet at high Weber numbers ($We_{jet} > 10^3$) is forced toward $\pi/2$.⁵⁹ As the remaining bubble volume continues to contract, the inner diameter of the toroidal bubble increases. This is accompanied by a decrease in the velocity of the convergent water jet

column, which stabilizes the annular outflow into a planar shape ($t > 42 \mu s$), also known as the smooth regime.⁵⁹ The vapor volume ejected by the reemergence of radial outflow at the bubble equator forms a highly irregular shape [Fig. 10(b) at $t = 43.0 \mu s$], detaching from the main bubble volume as the latter is still contracting and eventually collapses at $46.8 \mu s$ [Fig. 12(c)]. The characteristic collapse velocity of -10.8 m/s is thus reduced compared to the broad jet ($D^* = 1$) and mushroom-capped jet ($D^* = 0.7$) regimes, now similar to the unbounded case. The emitted shock wave from the primary collapse also induces a collapse of the outer volume [Fig. 12(c)], further fragmenting the shape of the remaining vaporous volume. The pressure peaks during the primary collapse are roughly 35% lower than in the case of a mushroom-capped jet regime ($D^* = 0.7$), indicating a significant reduction in bubble collapse strength with decreasing D^* .

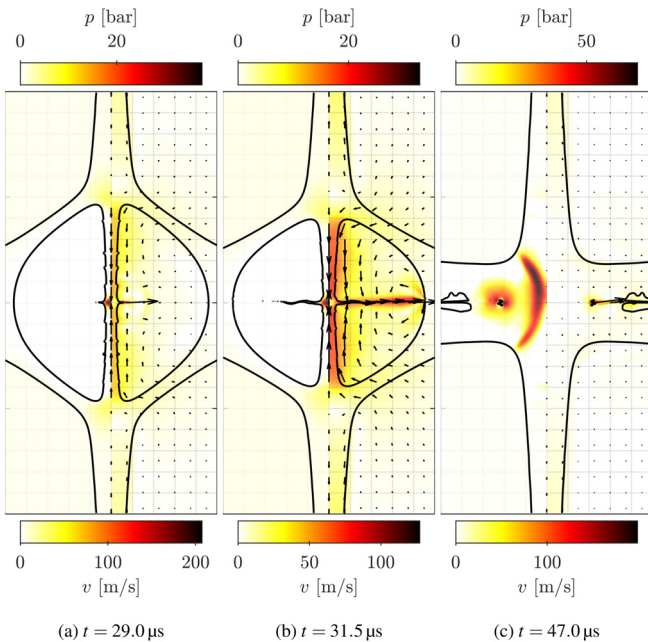


FIG. 12. Details behind (a) the impact of cylindrical jets ($D^* = 0.4$); (b) the resulting annular outflow; and (c) collapse of the main toroidal bubble. Shown are pressure (left) and velocity (right) contours. Phase interfaces are drawn with a solid black line. Width and height of each subfigure corresponds to 1 and 2 mm, respectively. Grid spacing is $100 \mu m$.

The rebounding and fragmented bubble volume continues to undergo several cycles of expansion and contraction, with increasingly pronounced breakup into a cloud of single oscillating bubbles. There is no clear evidence of secondary cavitation, which could be attributed to lesser collapse intensities with smaller values of parameter D^* , and the fact that subsequent collapses are not focused into singular events. This means that the remaining bubble clouds absorb and cushion the resulting pressure oscillations. On the other hand, the results from high-speed imaging do allow for a conclusive answer regarding the onset of secondary cavitation upon bubble creation. Some experimental repeats with a similar geometrical configuration hint toward the formation of an equatorial ring surrounding the expanding bubble. This coincides with the location of a horizontal plane where both reflected rarefaction waves constructively interfere. In some cases, the equatorial ring is not captured due to its short lifetime; however, we can still implicitly confirm it through observation of crater-like bubble wall irregularities around the time of maximum bubble expansion [Fig. 10(a) at $t = 26.5 \mu s$]. These irregularities are formed by the re-expanded remains of secondary cavitation, which are captured by the bubble wall during its explosive growth.^{44,60}

4. Thin cylindrical jets ($D^* = 0.25$)

Experimental and numerical image sequences of an even further bounded bubble ($d = 125 \mu\text{m}$ and $D^* = 0.25$) are shown in Figs. 13(a) (Multimedia view) and 13(b) (Multimedia view), respectively. During an explosive growth into an elongated volume, a very thin liquid film ($\approx 10 \mu\text{m}$) remains as a clear division between the bubble and the ambient air. As the vertical elongation of the bubble decelerates and the bubble further penetrates into the air layer, a thin liquid film continues propagating toward both bubble poles. The velocity difference between the shear flow of the liquid film and both bubble caps gradually develops, eventually (after $7 \mu\text{s}$) leading to the onset of a shape instability of the thin liquid layer [see video corresponding to Fig. 13(b) (Multimedia view)]. While the instabilities are evident on both the water–air and water–vapor interfaces, the former exhibits larger shape perturbations with a shorter wavelength, since there is roughly a 20-fold difference in the density ratio between both gaseous phases. This phenomenon can also be observed in previous experimental work [see image sequence in Fig. 12(e) by Rosselló *et al.*²³].

The peak vertical bubble elongation ($R_{\text{max}}^v = 968 \mu\text{m}$) reaches almost twice that of an equivalent spherical bubble and occurs immediately after the inversion of both bubble poles into jets at $t = 8.5 \mu\text{s}$. At that time, the counter jets also begin to form from the confluence of a thin shear flow along the bubble wall. Due to the onset of shape instabilities, the fronts of the counter jets exhibit shape irregularities, which further develop into fingers (after $10 \mu\text{s}$) that grow horizontally from the fronts of counter jets (air–water interface) propagating away from the bubble. Also here, the opposing axial jets initially form thin necks (radius $\sim 10 \mu\text{m}$) and mushroom caps that leave a trail of smaller droplets behind as a result of their breakdown. However, in this case, the droplets are not reattached to a thin neck of the jet as it progresses toward the bubble center, but rather remain enclosed within

the bubble [Fig. 13(b) at $t = 16.5 \mu\text{s}$]. Although the presently developed jets bear some resemblance to fast, thin jets⁶¹ (also called needle-jets³²) observed in bubbles evolving in the extreme vicinity of solid boundaries, they result from a fundamentally different way of flow focusing and reach speeds an order of magnitude below the sound speed of the ambient liquid.

The peak bubble volume ($R_{\text{max}}^{\text{eq}} = 448 \mu\text{m}$ at $11.3 \mu\text{s}$) is further reduced with increased boundedness of its environment. However, the opposite is true for the characteristic expansion velocity of 37.5 m/s , which is now 3.7 times that of an equivalent spherical bubble. With a mean speed of 123 m/s , the propagation of thin cylindrical jets through the bubble is sudden and briefly followed by their impact at $16.4 \mu\text{s}$. The impact occurs with jet speeds on the order of 150 m/s , inducing a strong pressure peak that momentarily surpasses 1000 bars. The impact results in partial atomization of both jet fronts and ejects small liquid droplets outward, toward the bubble wall. Also here, two opposing axially focused flows meet and are redirected radially, with the fronts of the annular outflow further breaking down into droplets [Fig. 14(a)]. Although outward directed droplets of both origins (jet impact and breakdown of a thin annular outflow) were not captured through high-speed imaging, we can implicitly confirm their existence from the experiments. In Fig. 13 at $t = 24.0 \mu\text{s}$, one can clearly see their emergence and disturbance of the remaining bubble volume in both experimental and numerical bubbles. In addition to front breakup, the annular outflow also exhibits a flapping shape instability, further aggravated when a bubble wall previously perturbed by the outwardly directed droplets is eventually inverted into axial jets and later redirected radially toward the bubble equator [Fig. 14(b)].

The remaining bubble volume undergoes further fragmentation during the contraction of a toroidal bubble part. The latter is penetrated by a progressively wider water column [Fig. 14(b)], causing its shape to eventually lose its resemblance of a needlelike shape. Multiple

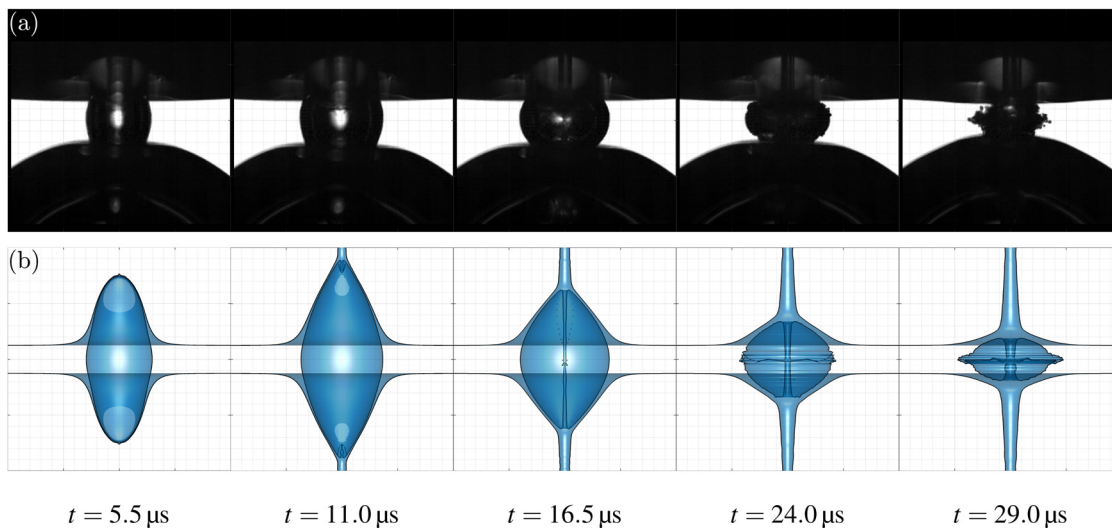


FIG. 13. Image sequence representing the thin cylindrical jet regime ($D^* = 0.25$): $R_{\text{max}}^h = 405 \mu\text{m}$, $t_{\text{max}}^h = 19.0 \mu\text{s}$, and $\Delta t_{\text{exp}} = \pm 1.47 \mu\text{s}$. (a) Experimental bubble ($R_{\text{max,exp}}^h = 522 \mu\text{m}$) and (b) simulated bubble: during explosive bubble expansion ($t = 5.5 \mu\text{s}$); after formation of thin cylindrical jets ($t = 11.0 \mu\text{s}$); at the time of jet impact ($t = 16.5 \mu\text{s}$); when the bubble wall is perturbed by the outwardly ejected water droplets, induced by jet impact and Plateau–Rayleigh instability of the water sheet tip ($t = 24.0 \mu\text{s}$); and during toroidal bubble contraction and further aggravation of the flapping shape instability of the water sheet ($t = 29.0 \mu\text{s}$). Width and height of each subfigure correspond to 2 mm . Minor grid spacing is $100 \mu\text{m}$. Numerical sequence shows volume fraction isosurfaces at $\alpha = 0.5$. Multimedia available online.

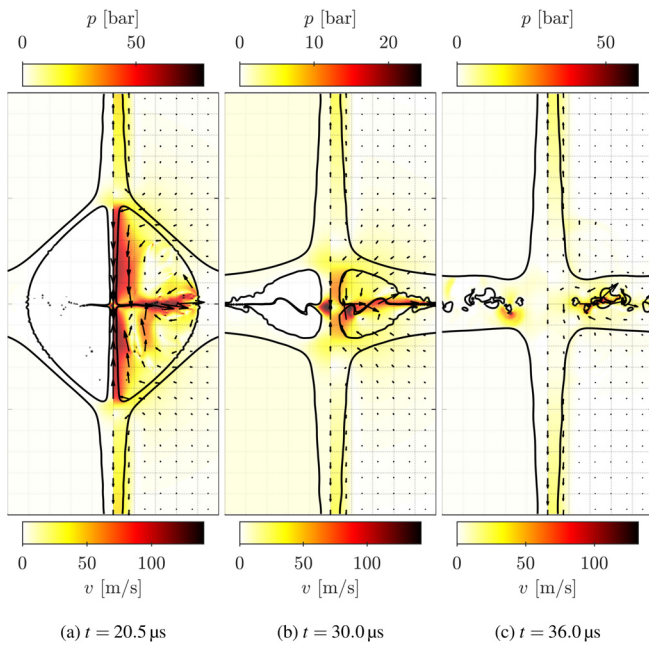


FIG. 14. Details behind (a) the impact of opposing thin jets ($D^* = 0.25$); (b) the resulting annular outflow; and (c) collapse of the main toroidal bubble. Shown are pressure (left) and velocity (right) contours. Phase interfaces are drawn with a solid black line. Width and height of each subfigure corresponds to 1 and 2 mm, respectively. Grid spacing is $100 \mu\text{m}$.

minor collapses are evident, with the main one identified at $t = 35.1 \mu\text{s}$, which, with a velocity of -10.4 m/s , yields the least violent characteristic collapse velocity of all cases considered. Bubble dynamics after the first collapse is qualitatively similar to the cylindrical jets regime

($D^* = 0.4$, see Sec. IV B 3). However, the remaining vaporous volume undergoes a faster transition into a cluster of clearly visible single bubbles, with fewer oscillation cycles. Again, there are no signs of secondary cavitation, except for the formation of an equatorial ring immediately after bubble inception.

5. Bubble atomization ($D^* = 0.15$)

At $D^* = 0.15$, the thickness of the liquid layer between both free surfaces amounts to $150 \mu\text{m}$, making it the most bounded scenario presently considered. The corresponding image sequences are gathered in Fig. 15(a) (Multimedia view) and Fig. 15(b) (Multimedia view), where it can be observed that at $t = 0.5 \mu\text{s}$, the expanding numerical bubble already protrudes well into the air phase with a thin liquid layer remaining between both gaseous phases. With the primary expansion of the bubble in the vertical direction, the liquid layer between the bubble and ambient air progressively thins and breaks up only $2 \mu\text{s}$ into the bubble's lifetime [Fig. 15(b) at $t = 2.0 \mu\text{s}$]. Bubble growth can be characterized as explosive and violent, with a mean expansion velocity of 99.8 m/s , almost ten times that of an equivalent unbounded bubble. The maximum bubble volume is reached already at $3 \mu\text{s}$ and is severely cushioned ($R_{\text{max}}^{\text{eq}} = 320 \mu\text{m}$) in comparison to other cases considered. At that time, both polar caps are detached from the thin liquid film and are completely atomized [Fig. 15(b) at $t = 2.5 \mu\text{s}$].

Following the rupture of the liquid film, the bubble contents are accelerated toward its center by the pressure difference between the ambient air compared to the internal bubble pressure. This results in the formation of two opposing broad air jets [Fig. 15(b) at $t = 4.5 \mu\text{s}$] that upon impact force the remaining bubble volume radially outward, toward the equator. This causes atomization of the bubble contents and mixing with the ambient air. The radially redirected mixture of vapor and air flows toward the equator of the cavity; however, it does not carry enough momentum to perturb the liquid interface. This is

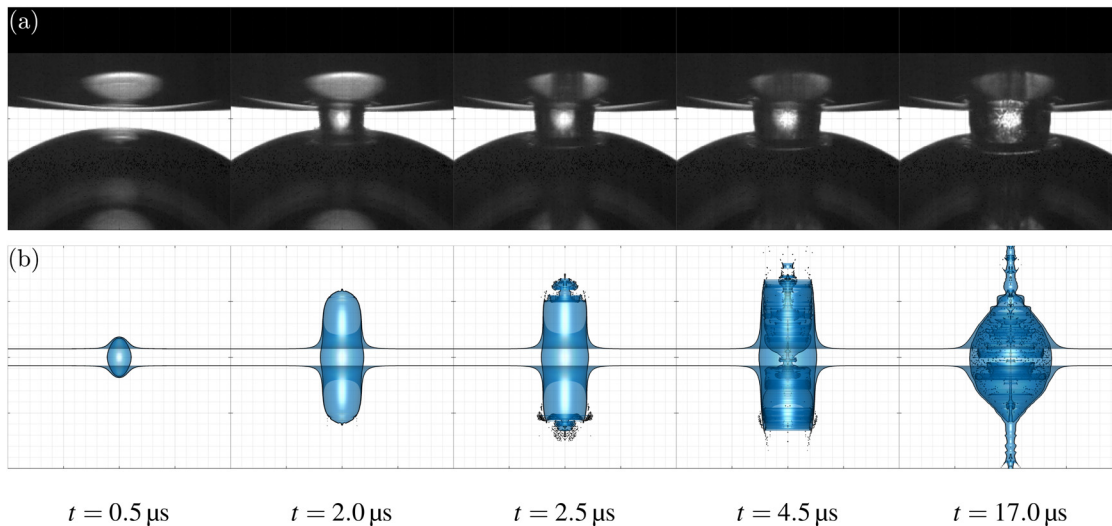


FIG. 15. Image sequence representing the bubble atomization regime ($D^* = 0.15$): $R_{\text{max}}^{\text{eq}} = 320 \mu\text{m}$, $t_{\text{max}}^{\text{eq}} = 2.96 \mu\text{s}$, and $\Delta t_{\text{exp}} = \pm 2.25 \mu\text{s}$. (a) Experimental bubble ($R_{\text{max,exp}}^h = 563 \mu\text{m}$) and (b) simulated bubble: during explosive bubble growth ($t = 0.5 \mu\text{s}$); at the beginning of a thin liquid film breakup ($t = 2.0 \mu\text{s}$); when ambient air accelerates bubble contents toward its center ($t = 2.5 \mu\text{s}$); upon impact of the opposing broad air jets ($t = 4.5 \mu\text{s}$); and after bubble contents are atomized and enclosed by an air-filled cavity ($t = 17.0 \mu\text{s}$). Width and height of each subfigure correspond to 2 mm. Minor grid spacing is $100 \mu\text{m}$. Numerical sequence shows volume fraction isosurfaces at $\alpha = 0.5$. Multimedia available online.

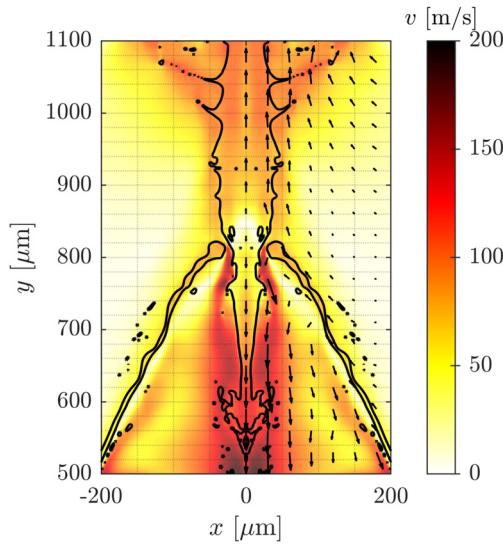


FIG. 16. Convergence of a broken liquid film at the axis of symmetry ($x = 0 \mu\text{m}$) results in cavity closure and the creation of a stagnation point ($y = 840 \mu\text{m}$), leading to the focusing of a thin water shell into a pair of divergent water jets. The primary axial jet is directed away from the cavity, while the remaining part of the flow is focused toward the center of the cavity. Phase interfaces (black solid line, $\alpha = 0.5$) and velocity field contours are shown at $t = 10.5 \mu\text{s}$.

also evident from the experimental images, as the wall of what falsely seems to be a bubble remains smooth at the equator. As a result, the vaporous and gaseous mixture is redirected again toward both vertical ends of a large cavity that remains in the place of a bubble.

Numerical results hint toward the development of a complex flow, rich in interfacial instabilities, which causes further atomization of the bubble contents, and is in line with previous research.^{23,44} Experimental sequences at 4.5 and 17 μs also suggest the atomized nature of the cavity's interior, while its edges around the equator remain smooth. After 8 μs , the broken liquid film eventually re-converges at the axis of symmetry, closing the predominantly air-filled cavity. This results in the creation of a stagnation point at the location of the cavity closure and leads to the focusing of the thin water shell into two pairs of divergent water jets. The primary axial jets are directed away from the cavity, whereas a part of the flow is focused toward the center of the cavity (Fig. 16).

While the resulting convergent water jets reach lower velocities (87.7 m/s) than the 146 m/s of thin cylindrical jets ($D^* = 0.25$, see Sec. IV B 4), they still occur as a result of a fundamentally similar

phenomenon of axial flow focusing, following the formation of a stagnation point at both bubble (cavity) poles. In the anisotropic scenario with a single free surface, this would lead to the formation of a so-called bullet jet.²³ However, presently, the inwardly directed water jets eventually impact each other, preventing the transfer of momentum further in the axial direction and thus the formation of a bullet jet. By that time, the vast majority of the vaporous bubble has condensed and the formed air-filled cavity remains semi-stable for a long period of time, beyond 800 μs from the bubble inception.

C. Water jets and sheets in imploding bubbles at null Kelvin impulse

Characteristics and dimensionless numbers of formed axial water jets in previously documented scenarios (Sec. IV B) with numerical bubbles at null Kelvin impulse are gathered in Table II. Here, r_{jet} , v_{jet} , and P_{jet} denote the characteristic jet radius, speed, and momentum, all defined at the instance of jet impact t_{jet} , whereas the time of the first bubble collapse is denoted by t_c . Jet radius is defined as a mean radial dimension of the water jet volume, i.e., a concave part of the bubble shape between its apex and the tip of the jet, whereas the tip velocity is considered as v_{jet} . On the other hand, the jet momentum is obtained by a volume integral over the whole jet volume. Re_{jet} and We_{jet} denote the Reynolds and Weber numbers of water jets, determined as $\text{Re}_{\text{jet}} = 2\rho_l v_{\text{jet}} r_{\text{jet}} / \mu_l$ and $\text{We}_{\text{jet}} = 2\rho_l v_{\text{jet}}^2 r_{\text{jet}} / \sigma_l$.

Overall, the developed axial jets get progressively thinner and faster with decreased D^* . This holds until a critical stand-off distance D_{crit}^* is reached, beyond which a liquid layer separating the bubble and ambient air is broken, leading to bubble atomization ($D^* = 0.15$) and the formation of slower water jets. We obtain D_{crit}^* to lie between 0.15 and 0.25, which is in good agreement with previous research.²³ The differences between jet characteristics span across an order of magnitude when D^* is decreased from unity to 0.25, yielding a roughly eightfold decrease in jet radius r_{jet} and a fivefold increase in impact velocity v_{jet} . On the other hand, the same cannot be said for jet momentum P_{jet} , which shows a nonuniform trend along D^* and roughly a fourfold reduction between the mushroom-capped jet ($D^* = 1$) and the thin cylindrical jet ($D^* = 0.25$). Based on the current results, we expect the fastest ($\sim 150 \text{ m/s}$) and thinnest ($\sim 0.03 R_{\text{max}}^h$) liquid jets just above D_{crit}^* at $D^* \approx 0.25$.

Since the fundamental jet-driving mechanisms remain unchanged for $D^* > D_{\text{crit}}^*$, one can reasonably expect a significant change in bubble characteristics preceding the jet formation to yield more than a fivefold increase in v_{jet} across the parameter space considered. The fundamental reasons behind this are twofold.

TABLE II. Characteristics and dimensionless numbers of formed axial water jets from numerical simulations.

Jetting regime	D_1^* (-)	t_c (μs)	t_{jet} (μs)	r_{jet} (μm)	v_{jet} (m s^{-1})	P_{jet} (kg m s^{-1})	Re_{jet} (10^3)	We_{jet} (10^3)	$r_{\text{jet}}/R_{\text{max}}^h$ (-)
Broad jet	1.00	70.2	66.8	101	27.5	1.47×10^{-7}	6.21	2.11	0.194
Mushroom-capped jet	0.70	61.7	51.9	79.1	34.0	1.96×10^{-7}	6.05	2.54	0.157
Cylindrical jet	0.40	46.8	28.7	30.2	77.7	1.03×10^{-7}	5.27	5.06	0.065
Thin cylindrical jet	0.25	35.1	16.4	13.0	146	0.48×10^{-7}	4.26	7.69	0.032

First, there exists a connection between jet formation and the curvature of the surface of aspherical bubbles, which is mediated by the concept of local flow focusing. This was established by Lechner *et al.*,²¹ who supported their claim by simulating the Rayleigh collapse of a prolate spheroidal bubble (see the Appendix C in Ref. 21). Their results demonstrated the formation of two convergent axial jets due to the inversion of both poles—the two most strongly curved parts of the bubble. Based on these results, the authors concluded that a bubble region with higher curvature collapses faster. This can be further explained by considering the Rayleigh equation, which describes the collapse of an empty spherical cavity. If taken at $\dot{R} = 0$, the bubble wall will accelerate proportionally to the reciprocal of R_{\max} : $\ddot{R} = -\frac{p_{\infty}}{\rho R_{\max}}$. This relation implies that the wall of a smaller bubble with higher curvature undergoes stronger acceleration than that of a larger bubble with lower curvature. Applying this argument locally to variably curved regions of a non-spherical bubble, one can recover the previous claim, effectively meaning that a deformed cavity exposed to overpressure will develop jets.

Second, bubbles in liquid drops exhibit shorter lifetimes than in extended liquid volumes, as shown by Obreschkow *et al.*⁶² Their work demonstrated that a spherical bubble centered in a liquid drop collapses faster than an unbounded spherical bubble with the same R_{\max} , indicating an additional effect of liquid film thickness on bubble wall acceleration. The authors also derived corrective terms for the Rayleigh–Plesset equation, which were validated with experimental data for bubbles half the size of the surrounding water drop. In its simplified form (Rayleigh equation) and at the time of R_{\max} ($\dot{R} = 0$), it reads: $\ddot{R} = -\frac{p_{\infty}}{\rho R_{\max}(1-\lambda)}$, with $\lambda(t) \equiv \frac{R(t)}{R_d(t)}$, where R_d denotes the drop radius. One can notice that a decrease in the liquid film thickness, $R_d - R$, yields a higher value of λ and thus higher bubble wall acceleration.

Both arguments translate to the presently considered phenomenon. Although surface tension and viscosity of the ambient liquid can affect jet formation and its characteristics, the phenomenon is still fundamentally governed by the collapse driving pressure $\Delta p = p_{\infty} - p_v$ and inertia. Due to the lower density of air in comparison to water, the bubbles created in a thin water layer will expand preferentially toward the water–air interface and deform into a prolate ellipsoid. As the thickness of the water layer decreases with a reduction in D^* , the bubble shape will assume progressively larger aspect ratios R^v/R^h . Thus, the primary reason for increased jet speeds with smaller D^* is the greater deformation of bubbles, leading to a higher local curvature κ_{pole} at the bubble region proximal to the free surface. Moreover, the finite thickness of the liquid film in the vertical direction compared to its effectively infinite horizontal dimension increases the bubble wall acceleration at the poles and thus further intensifies the effect of the bubble wall curvature on jet formation.

The obtained numerical results shown in the left-hand side of Fig. 17 conform to the given reasoning very well. The results also imply that $v_{\text{jet}} \propto \kappa_{\text{pole}}$; however, so far this can only be stated for a strong jetting regime, where the liquid film separating the bubble and ambient air remains intact ($D^*_{\text{crit}} < D^* \lesssim 1$). Presently, κ_{pole} and its reciprocal R_{pole} are considered as $\kappa_{\text{pole}} = \frac{1}{R_{\text{pole}}} \approx \frac{R^v_{\max}}{R^h{}^2}$, under an assumption of an ellipsoidal bubble shape. Horizontal bubble “radius” R^h is taken at the time of maximum vertical bubble expansion of R^v_{\max} .

In addition, the local radii of curvature R_{pole} in the right-hand side of Fig. 17 show a remarkable similarity to $D^* R^v_{\max}$, which

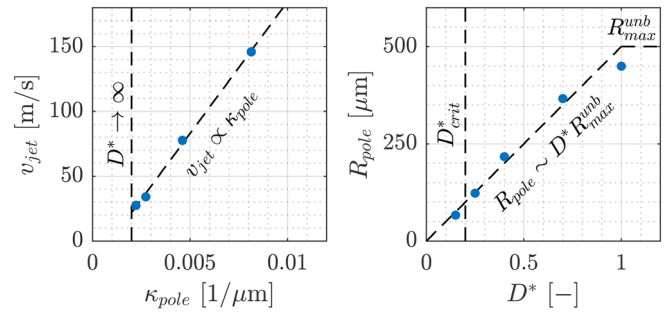


FIG. 17. Left: jet impact velocity v_{jet} is linearly proportional to the local curvature κ_{pole} at the bubble region proximal to the free surface (also pole). Right: local radii of curvature R_{pole} at the bubble pole in relation to D^* .

corresponds to the initial bubble-free surface stand-off distance d , and further implies a linear relationship between D^* and v_{jet} . Interestingly, the similarity $R_{\text{pole}} \sim D^* R^v_{\max}$ holds even beyond D^*_{crit} , in the bubble atomization regime ($D^* = 0.15$); however, it has to be stated that there the jet characteristics are governed by the closure of a water bell, after the bubble has been atomized and the formed cavity is vented. This causes an almost nullification of the collapse driving pressure, which is an additional reason behind the lower speeds of water jets in the bubble atomization regime ($v_{\text{jet}} \approx 85$ m/s at $D^* = 0.15$, not shown in Fig. 17). Conversely, for $D^* \gtrsim 1$, the R_{pole} approaches R^v_{\max} , which is to be expected as the bubbles are progressively less deformed from the spherical shape of an unbounded case.

We revisit the jet dimensionless numbers gathered in Table II. These values are reported at the time of impact t_{jet} and due to their transient nature change significantly during their lifetime. Both the jet Reynolds numbers Re_{jet} and the corresponding Weber numbers We_{jet} are on the order of a few thousand, which further points toward a minor influence of surface tension and viscous forces on the overall jetting phenomena. While Re_{jet} monotonically increases with D^* , an opposite trend is found for We_{jet} . The latter is especially important as it determines the flow regime of the liquid sheet (also referred to as annular outflow) proceeding the convergent jet impact.

Previous research on water sheets, produced when the ejection angle of a water jet is forced toward $\pi/2$,⁵⁹ points to the existence of two characteristic flow regimes: smooth and flapping regime. Their onset is dependent on We_{jet} , with a transition between both regimes occurring at the critical Weber number $\text{We}_{\text{jet}}^{\text{crit}}$. In the present case, we encounter the onset of a flapping regime with a transition between the mushroom-capped ($D^* = 0.7$, $\text{We}_{\text{jet}} \approx 2500$) and cylindrical ($D^* = 0.4$, $\text{We}_{\text{jet}} \approx 5000$) jets. However, one must consider that presently a thin water sheet is entrapped within a vaporous bubble with the density roughly 30-times lower than air at standard atmospheric conditions, for which $\text{We}_{\text{jet}}^{\text{crit}} \approx 1000$ was reported.⁵⁹ Since $\text{We}_{\text{jet}}^{\text{crit}}$ is proportional to the square root of the liquid to gas density ratio, this presently implies $\text{We}_{\text{jet}}^{\text{crit}} \approx 5500$ and corresponds well to the obtained results, especially when one considers that here encountered jets are highly transient.

Further attention is given to the temporal evolution of jet characteristics reported in Table II. For direct comparison, a set of supplementary simulations considering anisotropic scenarios with a single free surface ($D^*_2 = \infty$) was conducted for $D^*_1 = [0.25, 1]$ and the

TABLE III. Characteristics and dimensionless numbers of formed axial water jets from numerical simulations of anisotropic configurations with a single free boundary.

Jetting regime	D_1^* (-)	t_c (μs)	t_{jet} (μs)	r_{jet} (μm)	v_{jet} (m s^{-1})	P_{jet} (kg m s^{-1})	Re_{jet} (10^3)	We_{jet} (10^3)	$r_{\text{jet}}/R_{\text{max}}^h$ (-)
Broad jet	1.00	79.0	78.7	154	34.1	6.89×10^{-7}	11.8	4.98	0.299
Mushroom-capped jet	0.70	74.1	66.3	105	34.5	6.22×10^{-7}	8.10	3.46	0.206
Cylindrical jet	0.40	66.1	36.2	34.8	76.6	2.24×10^{-7}	5.99	5.67	0.072
Thin cylindrical jet	0.25	61.5	20.3	15.4	143	0.96×10^{-7}	4.95	8.77	0.034

results are gathered in Table III. Overall, the results of the supplementary simulations show a high level of qualitative similarity between both scenarios, indicating that in both configurations, the jets originate from the same fundamental mechanism of axial flow focusing. Jets develop similar shape features and instabilities, justifying their classification into the same jetting regime. Obviously, the similarities in bubble and jetting dynamics cease after the time of jet impact t_{jet} due to the symmetric nature of a null Kelvin impulse environment.

We observe that jet radii at null Kelvin impulse are consistently reduced in comparison to the corresponding cases with a single free surface. In the anisotropic scenario ($D_2^* = \infty$), the formed broad ($D_1^* = 1$) and mushroom-capped ($D_1^* = 0.7$) jets attain roughly 30% and 20% of R_{max}^h , which is significantly more than approximately 19% and 16% in the corresponding null Kelvin impulse environments with two opposing free surfaces. Similarly, jet momentum exhibits a twofold difference for thin cylindrical jets, which increases consistently with larger D_1^* and reaches almost a fivefold difference at $D_1^* = 1$. However, this is not the case for v_{jet} , where the relative differences between both configurations become negligible (<2%) for mushroom-capped, cylindrical, and thin cylindrical jets.

The primary reason behind the apparent quantitative differences in the observed characteristics of jets, when compared to the corresponding scenarios with a single free surface, becomes evident when one compares their temporal evolution in Fig. 18. Comparisons are provided for the four considered scenarios with D^* ranging from 1 to 0.25, where the liquid layer separating both gaseous phases remains intact, thereby preventing the atomization of the vaporous bubble and the formation of a vented cavity. First, we compare the locations y_{tip} of both bubble tips along the axis of symmetry in the top row of Fig. 18. They are obtained as intersections of the bubble shape ($\alpha_v = 0.5$) with the axis of symmetry. As long as the bubble shape remains convex, these two points mark the extent of the bubble shape in the vertical direction; however, as the tips invert and jets are formed (dot markers), the curves describe the propagation of jet fronts. Observing the propagation of the upper tips (solid lines), one can notice that the curves practically overlap at $D_1^* = 1$. While a gradually increasing offset is evident with smaller stand-off distances, the differences remain relatively small. This also holds for the time of jet formation, which remains within a difference of $0.5 \mu\text{s}$ even in the regime of thin cylindrical jets. These results imply that the dynamics of the proximal bubble tips (solid lines), and later jet fronts, is practically unaffected by the characteristics of the bubble environment on the opposite side. However, it is important to stress that this is only true until the occurrence of jet impact (asterisk marker). A similar conclusion can be drawn from the dynamics of the lower bubble tips (dashed lines). In all four cases, the south tips (blue dashed line) of anisotropically bounded bubbles

($D_2^* = \infty$) closely follow the trajectory of an equivalent spherical bubble (black dashed line). Only after $t \approx 45 \mu\text{s}$, when the bubble begins to contract along the axis of symmetry, minor differences emerge as the distal tip accelerates faster than in the unbounded bubble. However, this is relevant only in the broad jet and mushroom-capped jet regime of anisotropically bounded bubbles, as the developed cylindrical jets already pierce the opposite bubble wall while it is still in the phase of vertical expansion.

A high level of quantitative agreement can also be observed between isotropically ($D_2^* = D_1^*$, orange color) and anisotropically ($D_2^* = \infty$, blue color) bounded bubbles when comparing the propagation velocities of jet tips in the second row of Fig. 18. In all four jetting regimes, the lines practically overlap, indicating a minor effect of D_2^* until jet impact occurs in the considered configurations. This also implies that the main reason for quantitative differences in characteristic jet impact velocities v_{jet} between both broad jet configurations ($D_1^* = 1$) is that broad jets at null Kelvin impulse have a shorter lifespan. This is because they are met by a symmetrically opposing counter jet at the bubble center, limiting their time under acceleration compared to the corresponding anisotropic environment and thus reducing the attained impact velocity.

On the other hand, the differences in v_{jet} among the other considered jetting scenarios are only on the order of a few percent. As the jets become faster and thinner, it is noticeable that the bulk of their acceleration occurs before the jet tip reaches the central horizontal plane ($y=0$). Furthermore, the acceleration of thin cylindrical jets ($D^* = 0.25$) is briefly halted after $12 \mu\text{s}$ when they lose their unstable mushroom-shaped caps and reach a speed of 150 m/s . In this case, minor discrepancies in jet front velocities are evident between 10 and $12 \mu\text{s}$. A closer examination of the video corresponding to Fig. 13(b) (Multimedia view) reveals that at that time, the jet tips are highly affected by the onset of the Rayleigh–Taylor instability, and that the fronts the opposing thin cylindrical jets do not exactly mirror each other during their propagation through the bubble. This discrepancy could be attributed to numerical errors that accumulate when the jet tips are partially broken down into small fragments, close to the employed spatial resolution of $1.25 \mu\text{m}$. An even greater drawback may be the reinforcement of axial symmetry, which poses an additional limitation on adequately resolving the predicted small-scale instabilities. However, achieving spatially adequate and three-dimensional resolution for the considered problem currently imposes computational demands far beyond our capacity.

The temporal progressions of jet radii r_{jet} in the bottom row of Fig. 18 also exhibit a remarkable level of similarity between isotropic ($D_1^* = D_2^*$, orange) and anisotropic ($D_2^* = \infty$, blue) scenarios. Monotonically increasing trends in the temporal evolution of r_{jet} are

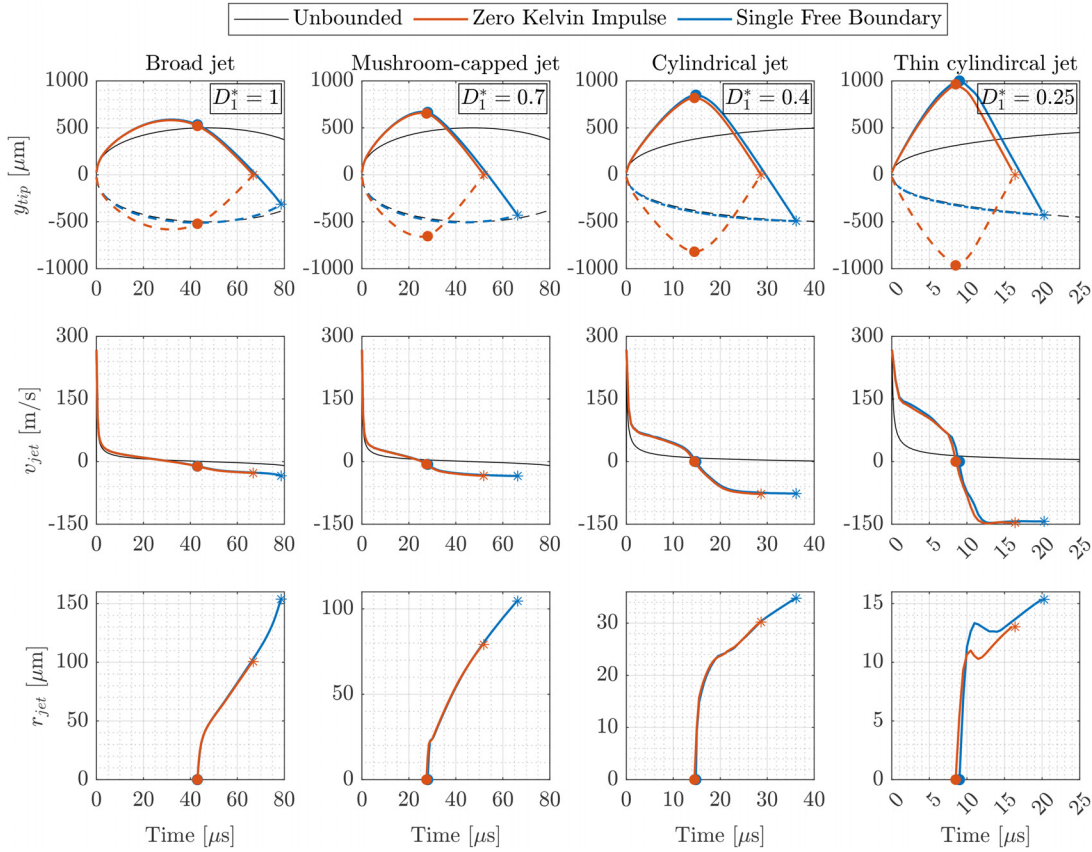


FIG. 18. Temporal progression of the vertical location (y_{tip} , first row) of the upper (solid line) and lower (dashed line) bubble tip, their velocities (v_{jet} , second row), and the resulting radii of the formed uniaxial jets (r_{jet} , third row). Shown are numerical results for null Kelvin impulse configurations (orange) and the corresponding cases with a single free surface ($D_2^* = \infty$, blue). The dynamics of an equivalent unbounded bubble ($R_{max}^{unb} = 500 \mu\text{m}$ and $\mu_c^{unb} = 93.9 \mu\text{s}$) is included for reference (black solid line). Each column corresponds to an unique bubble jetting regime (from the left to the right): broad jet ($D^* = 1$), mushroom-capped jet ($D^* = 0.7$), cylindrical jet ($D^* = 0.4$), and thin cylindrical jet ($D^* = 0.25$). Markers denote the time of jet formation (dot) and impact (asterisk).

evident for $D^* \geq 0.4$, implying that jets progressively widen during their lifetime. This also holds for the thin cylindrical jetting regime; however, there a local maximum is followed by a temporary reduction of r_{jet} , which occurs due to the breakdown and rounding of the jet tip. While an accelerated widening of the broad jets (convex curves after $50 \mu\text{s}$) is observed, the rest exhibits a decelerated rate of radial growth in the final stage before the jet impact.

Overall, the results for bubbles induced in a liquid layer suggest a negligible effect of the distal bubble environment (D_2^*) on the dynamics of the developed axial jet proximal to the liquid–air interface. However, this ceases to be valid after the time of jet impact, where the resulting flow will be highly dependent on the net anisotropy of the overall bubble environment. At null Kelvin impulse, the latter amounts to zero, resulting in an impact of two opposite equal jets at the central plane. After the impact, the net flow is redirected radially and diverges as a liquid sheet. With smaller stand-offs D^* and thus higher characteristic jet velocities v_{jet} , the impact intensity and the resulting pressure peaks are increased. Flow diversion is accompanied by an abruptly accelerated circular edge, which can reach velocities beyond 1000 m/s before its shape reverses outward. This reversal is extremely

short-lived ($\ll 1 \mu\text{s}$) and is followed by an instant deceleration of the flow by an order of magnitude. The thickness of the liquid sheet tip is on the order of a micrometer, leading to the onset of the Plateau–Rayleigh instability and its breakup into smaller droplets before it reemerges at the bubble equator. Additionally, stronger impacts of cylindrical and thin cylindrical jets with $We_{jet} > 5000$ also induce a shape instability of the liquid sheet, characteristic of the so-called flapping regime.

Due to the very small scales of the numerically observed instabilities and their confinement within the bubble, we were only able to indirectly confirm their existence through experimental observation of irregularities at the bubble wall resulting from the impact and protrusion of the atomized water droplets. We also acknowledge that the predicted instabilities do not necessarily conform to axial symmetry, potentially affecting the validity of the obtained numerical results. However, a comparison with experimental data demonstrates a good overall agreement with numerical simulations, even after the occurrence of jet impact. The most significant quantitative disagreement that occurs between the time of jet impact and bubble collapse is the numerical overprediction of the strength of the annular outflow (also

referred to as a liquid sheet). This overprediction causes an excessive widening of the bubble volume after it reemerges at the equator and grows with an increasing boundedness of the bubble environment (smaller D^*). We attribute the observed discrepancies primarily to the enforcement of axial symmetry, which artificially over-stabilizes the inherently unstable annular outflow. For instance, the tip of the water sheet is expected to break into droplets rather than axially symmetric rings. Their spatial scale poses an additional source of error compared to the employed spatial resolution of 1.25 μm .

V. CONCLUSIONS

In this work, we experimentally and numerically investigated the dynamics of a single laser-induced cavitation bubble in a thin liquid layer. Highly bounded environments at dimensionless stand-off bubble-free surface distances D^* below unity were considered. Additionally, we imposed the condition of null Kelvin impulse, subjecting the bubble to the oppositely equal influence of two opposing free surfaces.

We considered macro-scale bubbles with the maximum diameter on the order of a millimeter. The experimental bubbles were induced by focusing a pulsed laser into a liquid layer and their dynamics was captured using high-speed imaging. Numerical simulations were used to provide further insight into the considered phenomena, using a Finite volume method-based solver. The numerical methodology considered compressible and viscous multiphase flow, modeled according to the volume of fluid approach.

Overall, a good agreement was found between the experimental and numerical results. We observed a diverse spectrum of bubble jetting phenomena, encompassing broad jets ($D^* = 1$), mushroom-capped jets ($D^* = 0.7$), cylindrical jets ($D^* = 0.4$), and thin cylindrical jets ($D^* = 0.25$). Jets were found to become progressively thinner and faster with smaller bubble-free surface stand-off distances D^* , reaching radii down to 3% of the maximal bubble radius and speeds up to 150 m/s. In addition to mushroom-capped jets, mushroom-shaped caps formation was also observed in cylindrical and thin cylindrical jets. However, in both regimes, the mushroom caps are unstable and break up due to the onset of the Rayleigh–Taylor instability, leading to tip rounding before the jet impact.

The obtained results imply a linear relationship between the jet impact velocity and the local curvature at the bubble region proximal to the free surface (also pole), suggesting that the magnitude of bubble deformation during its growth phase is the primary factor influencing the observed fivefold increase in the jet impact velocity across the parameter space considered. In addition, we found a remarkable similarity of the local curvature at the bubble pole to the reciprocal of $D^* R_{\text{max}}^{\text{umb}}$, which corresponds to the initial bubble-free surface stand-off distance, and further implies a linear relationship between D^* and jet impact velocity.

Our findings showed that bubble collapse intensity is progressively dampened with increased boundedness of its environment. The opposite trend was found for the impact intensity of convergent axial jets, resulting in local pressure transients up to 100 MPa and triggering the formation of a fast and thin annular outflow in the form of a liquid sheet, affected by the Rayleigh–Plateau and flapping shape instability. As D^* decreases beyond a critical value, estimated between $D^* = 0.15$ and 0.25, the liquid layer separating the bubble and ambient air thins, leading to the onset of interfacial shape instabilities, its breakdown, and bubble atomization.

Finally, we compared bubbles at zero Kelvin impulse to corresponding anisotropic scenarios with a single free surface, revealing that the dynamics of axial jets until the time of impact is primarily influenced by the proximal free surface, yielding an increased bubble shape elongation with a reduction in the liquid layer thickness.

ACKNOWLEDGMENTS

The authors acknowledge the financial support from the European Research Council under the European Union’s

TABLE IV. The considered values of material parameters.^{64,65}

Parameter (unit)	Value
R_{gas} (J kmol ⁻¹ K ⁻¹)	8.31×10^3
p_{ref} (Pa)	3.17×10^3
T_{ref} (K)	298
Bubble–vapor	
μ_v (Pa s)	9.70×10^{-6}
λ_v (W m ⁻¹ K ⁻¹)	1.84×10^{-2}
M_v (kg kmol ⁻¹)	18.0
$h_{\text{ref}v}$ (J kg ⁻¹)	2.55×10^6
C_{vv} (J kg ⁻¹ K ⁻¹)	$f(T)$
Liquid–water	
μ_l (Pa s)	8.90×10^{-4}
λ_l (W m ⁻¹ K ⁻¹)	6.07×10^{-1}
σ_l (N m ⁻¹)	7.20×10^{-2}
γ_l (-)	1.19
C_{vl} (J kg ⁻¹ K ⁻¹)	3.61×10^3
$P_{\infty l}$ (Pa)	6.22×10^8
b_l (m ³ kg ⁻¹)	6.72×10^{-4}
q_l (J kg ⁻¹)	-1.18×10^6
Gas–air	
μ_g (Pa s)	1.85×10^{-5}
λ_g (W m ⁻¹ K ⁻¹)	2.55×10^{-2}
M_g (kg kmol ⁻¹)	29.0
$h_{\text{ref}g}$ (J kg ⁻¹)	0
C_{vg} (J kg ⁻¹ K ⁻¹)	719

TABLE V. The considered values of NASA Glenn thermodynamic data coefficients $a_{j,k}$ used for calculation of C_{pv} .⁶³

$a_{j,k}$	j		Unit
	1	2	
-2	-3.95×10^4	1.04×10^6	K ²
-1	5.76×10^2	-2.41×10^3	K ¹
0	9.32×10^{-1}	4.65×10^0	...
k	1	7.22×10^{-3}	K ⁻¹
	2	-7.34×10^{-6}	K ⁻²
	3	4.96×10^{-9}	K ⁻³
	4	-1.34×10^{-12}	K ⁻⁴

05 December 2024 09:17:57

Framework Program for research and innovation, Horizon 2020 (Grant Agreement No. 771567—CABUM), the European Union's Marie Skłodowska-Curie postdoctoral fellowship (Grant Agreement No. 101064097—NASCAP), Alexander von Humboldt Foundation (Friedrich Wilhelm Bessel Research Award Programme, 2019), and the Slovenian Research and Innovation Agency (core Funding No. P2-0422, Project Nos. Z2-50062 and J2-3057).

AUTHOR DECLARATIONS

Conflict of Interest

The authors have no conflicts to disclose.

Author Contributions

Jure Zevnik: Conceptualization (equal); Data curation (equal); Formal analysis (equal); Funding acquisition (equal); Investigation (equal); Methodology (equal); Supervision (equal); Visualization (equal); Writing – original draft (equal); Writing – review & editing (equal). **Julien Patfoort:** Investigation (equal). **Juan Manuel Rosselló:** Funding acquisition (equal); Methodology (equal); Supervision (equal); Writing – review & editing (equal). **Claus-Dieter Ohl:** Conceptualization (equal); Writing – review & editing (equal). **Matevž Dular:** Conceptualization (equal); Funding acquisition (equal); Investigation (equal); Supervision (equal); Writing – review & editing (equal).

DATA AVAILABILITY

The data that support the findings of this study are available from the corresponding author upon reasonable request.

APPENDIX: THE CONSIDERED MATERIAL PARAMETERS

The considered values of material parameters rounded to the first three significant digits are given in Table IV. The remaining material parameters for both gaseous phases ($i = v, g$ denotes the vapor and gas phase, respectively) are obtained from the relations in Eq. (A1).^{47,48,63} The employed values of parameters $a_{j,k}$ for calculation of C_{pv} are gathered in Table V.

$$\begin{aligned}
 R_i^* &= \frac{R_{gas}}{M_i}, \\
 C_{pv} &= \begin{cases} R_v^* \sum_{k=-2}^4 a_{1,k} T^k, & 200 \text{ K} \leq T \leq 1000 \text{ K}, \\ R_v^* \sum_{k=-2}^4 a_{2,k} T^k, & 1000 \text{ K} < T \leq 6000 \text{ K}, \end{cases} \\
 C_{vi} &= C_{pi} - R_i^*, \\
 \gamma_i &= \frac{C_{pi}}{C_{vi}}, \\
 e_{ref i} &= h_{ref i} - R_i^* T_{ref}.
 \end{aligned} \tag{A1}$$

REFERENCES

- T. B. Benjamin and A. T. Ellis, "A discussion on deformation of solids by the impact of liquids, and its relation to rain damage in aircraft and missiles, to blade erosion in steam turbines, and to cavitation erosion—The collapse of cavitation bubbles and the pressures thereby produced," *Philos. Trans. R. Soc. London, Ser. A* **260**, 221–240 (1966).
- T. Ikeda, S. Yoshizawa, N. Koizumi, M. Mitsuishi, and Y. Matsumoto, "Focused ultrasound and lithotripsy," *Adv. Exp. Med. Biol.* **880**, 113–129 (2016).
- C. E. Brennen, "Cavitation in medicine," *Interface Focus* **5**, 20150022 (2015).
- P. R. Gogate, "Cavitational reactors for process intensification of chemical processing applications: A critical review," *Chem. Eng. Process.* **47**, 515–527 (2008).
- T. J. Mason and P. Cintas, "Sonochemistry," in *Handbook of Green Chemistry and Technology* (Wiley, 2002), pp. 372–396.
- P. R. Gogate and A. B. Pandit, "A review of imperative technologies for wastewater treatment I: Oxidation technologies at ambient conditions," *Adv. Environ. Res.* **8**, 501–551 (2004).
- M. Dular, T. Griessler-Bulc, I. Gutierrez-Aguirre, E. Heath, T. Kosjek, A. Krivograd Klemencič, M. Oder, M. Petkovšek, N. Rački, M. Ravnikar, A. Šarc, B. Širok, M. Zupanc, M. Žitnik, and B. Kompore, "Use of hydrodynamic cavitation in (waste)water treatment," *Ultrason. Sonochem.* **29**, 577–588 (2016).
- S. L. Ceccio, "Friction drag reduction of external flows with bubble and gas injection," *Annu. Rev. Fluid Mech.* **42**, 183–203 (2010).
- S. P. Wang, A. M. Zhang, Y. L. Liu, S. Zhang, and P. Cui, "Bubble dynamics and its applications," *J. Hydrodyn.* **30**, 975–991 (2018).
- A. Philipp and W. Lauterborn, "Cavitation erosion by single laser-produced bubbles," *J. Fluid Mech.* **361**, 75–116 (1998).
- M. Dular, T. Požar, J. Zevnik, and R. Petkovšek, "High speed observation of damage created by a collapse of a single cavitation bubble," *Wear* **418–419**, 13–23 (2019).
- Z. Zeng, S. R. Gonzalez-Avila, R. Dijkink, P. Koukouvinis, M. Gavaises, and C. D. Ohl, "Wall shear stress from jetting cavitation bubbles," *J. Fluid Mech.* **846**, 341–355 (2018).
- J. Zevnik and M. Dular, "Cavitation bubble interaction with compliant structures on a microscale: A contribution to the understanding of bacterial cell lysis by cavitation treatment," *Ultrason. Sonochem.* **87**, 106053 (2022).
- E. B. Flint and K. S. Suslick, "The temperature of cavitation," *Science* **253**, 1397–1399 (1991).
- K. S. Suslick, W. B. McNamara, and Y. Didenko, "Hot spot conditions during multi-bubble cavitation," in *Sonochemistry and Sonoluminescence* (Springer Science & Business Media, 1999), pp. 191–204.
- W. Lauterborn and A. Vogel, "Shock wave emission by laser generated bubbles," in *Bubble Dynamics and Shock Waves* (Springer Berlin Heidelberg, Berlin, Heidelberg, 2013), pp. 67–103.
- M. Petkovšek, M. Hočevar, and M. Dular, "Visualization and measurements of shock waves in cavitating flow," *Exp. Therm. Fluid Sci.* **119**, 110215 (2020).
- K. S. Suslick, "Sonochemistry," *Science* **247**, 1439–1445 (1990).
- D. Podbevšek, G. Ledoux, and M. Dular, "Investigation of hydrodynamic cavitation induced reactive oxygen species production in microchannels via chemiluminescent luminol oxidation reactions," *Water Res.* **220**, 118628 (2022).
- W. Lauterborn and C. D. Ohl, "Cavitation bubble dynamics," *Ultrason. Sonochem.* **4**, 65–75 (1997).
- C. Lechner, W. Lauterborn, M. Koch, and R. Mettin, "Jet formation from bubbles near a solid boundary in a compressible liquid: Numerical study of distance dependence," *Phys. Rev. Fluids* **5**, 093604 (2020).
- P. Koukouvinis, M. Gavaises, O. Supponen, and M. Farhat, "Numerical simulation of a collapsing bubble subject to gravity," *Phys. Fluids* **28**, 032110 (2016).
- J. M. Rosselló, H. Reese, and C. D. Ohl, "Dynamics of pulsed laser-induced cavities on a liquid–gas interface: From a conical splash to a 'bullet' jet," *J. Fluid Mech.* **939**, A35 (2022).
- B. Han, K. Köhler, K. Jungnickel, R. Mettin, W. Lauterborn, and A. Vogel, "Dynamics of laser-induced bubble pairs," *J. Fluid Mech.* **771**, 706–742 (2015).
- J. M. Rosselló, W. Lauterborn, M. Koch, T. Wilken, T. Kurz, and R. Mettin, "Acoustically induced bubble jets," *Phys. Fluids* **30**, 122004 (2018).
- J. R. Blake, D. M. Leppinen, and Q. Wang, "Cavitation and bubble dynamics: The Kelvin impulse and its applications," *Interface Focus* **5**, 20150017 (2015).
- O. Supponen, D. Obreschkow, M. Tinguely, P. Kobel, N. Dorsaz, and M. Farhat, "Scaling laws for jets of single cavitation bubbles," *J. Fluid Mech.* **802**, 263–293 (2016).
- Z. Pandur, J. Zevnik, D. Podbevšek, B. Stojković, D. Stopar, and M. Dular, "Water treatment by cavitation: Understanding it at a single bubble - bacterial cell level," *Water Res.* **236**, 119956 (2023).
- J. R. Blake, "The Kelvin impulse: Application to cavitation bubble dynamics," *J. Aust. Math. Soc. Ser. B, Appl. Math.* **30**, 127–146 (1988).

- ³⁰D. Obreschkow, M. Tinguely, N. Dorsaz, P. Kobel, A. de Bosset, and M. Farhat, "Universal scaling law for jets of collapsing bubbles," *Phys. Rev. Lett.* **107**, 204501 (2011).
- ³¹M. Koch, J. M. Rosselló, C. Lechner, W. Lauterborn, J. Eisener, and R. Mettin, "Theory-assisted optical ray tracing to extract cavitation-bubble shapes from experiment," *Exp. Fluids* **62**, 60 (2021).
- ³²F. Reuter and C.-D. D. Ohl, "Supersonic needle-jet generation with single cavitation bubbles," *Appl. Phys. Lett.* **118**, 134103 (2021).
- ³³J. Mur, V. Agrež, J. Zevnik, R. Petkovšek, and M. Dular, "Microbubble collapse near a fiber: Broken symmetry conditions and a planar jet formation," *Phys. Fluids* **35**, 023305 (2023).
- ³⁴A. B. Sieber, D. B. Preso, and M. Farhat, "Cavitation bubble dynamics and microjet atomization near tissue-mimicking materials," *Phys. Fluids* **35**(2), 027101 (2023).
- ³⁵J. R. Blake and D. C. Gibson, "Cavitation bubbles near boundaries," *Annu. Rev. Fluid Mech.* **19**, 99–123 (1987).
- ³⁶D. Mnich, F. Reuter, F. Denner, and C.-D. Ohl, "Single cavitation bubble dynamics in a stagnation flow," *J. Fluid Mech.* **979**, A18 (2024).
- ³⁷J. R. Blake, B. B. Taib, and G. Doherty, "Transient cavities near boundaries. Part 1. Rigid boundary," *J. Fluid Mech.* **170**, 479–497 (1986).
- ³⁸A. Shima, Y. Tomita, D. C. Gibson, and J. R. Blake, "The growth and collapse of cavitation bubbles near composite surfaces," *J. Fluid Mech.* **203**, 199–214 (1989).
- ³⁹P. A. Quinto-Su, K. Y. Lim, and C.-D. Ohl, "Cavitation bubble dynamics in microfluidic gaps of variable height," *Phys. Rev. E* **80**, 047301 (2009).
- ⁴⁰B. Liu, J. Cai, and X. Huai, "Heat transfer with the growth and collapse of cavitation bubble between two parallel heated walls," *Int. J. Heat Mass Transfer* **78**, 830–838 (2014).
- ⁴¹S. R. Gonzalez-Avila, E. Klaseboer, B. C. Khoo, and C.-D. Ohl, "Cavitation bubble dynamics in a liquid gap of variable height," *J. Fluid Mech.* **682**, 241–260 (2011).
- ⁴²E. Robert, J. Lettry, M. Farhat, P. A. Monkewitz, and F. Avellan, "Cavitation bubble behavior inside a liquid jet," *Phys. Fluids* **19**(6), 067106 (2007).
- ⁴³J. Zhou and M. Andersson, "An analysis of surface breakup induced by laser-generated cavitation bubbles in a turbulent liquid jet," *Exp. Fluids* **61**, 242 (2020).
- ⁴⁴J. M. Rosselló, H. Reese, K. A. Raman, and C.-D. Ohl, "Bubble nucleation and jetting inside a millimetric droplet," *J. Fluid Mech.* **968**, A19 (2023).
- ⁴⁵W. Lauterborn, C. Lechner, M. Koch, and R. Mettin, "Bubble models and real bubbles: Rayleigh and energy-deposit cases in a Tait-compressible liquid," *IMA J. Appl. Math.* **83**, 556–589 (2018).
- ⁴⁶ANSYS® Fluent, Release 22.2, 2022, ANSYS, Inc.
- ⁴⁷O. Le Métayer and R. Saurel, "The Noble-Abel Stiffened-Gas equation of state," *Phys. Fluids* **28**, 046102 (2016).
- ⁴⁸A. Chiapolino and R. Saurel, "Extended Noble-Abel Stiffened-gas equation of state for sub-and-supercritical liquid-gas systems far from the critical point," *Fluids* **3**, 48 (2018).
- ⁴⁹W. H. Lee, "Pressure iteration scheme for two-phase flow modeling," in *Multiphase Transport Fundamentals, Reactor Safety, Applications*, edited by T. Veziroglu (Hemisphere Publishing, Washington, DC, 1980), pp. 407–432.
- ⁵⁰I. Akhatov, O. Lindau, A. Topolnikov, R. Mettin, N. Vakhitova, and W. Lauterborn, "Collapse and rebound of a laser-induced cavitation bubble," *Phys. Fluids* **13**, 2805–2819 (2001).
- ⁵¹A. Vogel, S. Busch, and U. Parlitz, "Shock wave emission and cavitation bubble generation by picosecond and nanosecond optical breakdown in water," *J. Acoust. Soc. Am.* **100**, 148–165 (1996).
- ⁵²E. W. Lemmon, I. H. Bell, M. L. Huber, and M. O. McLinden, "Thermophysical properties of fluid systems" in *NIST Chemistry WebBook*, NIST Standard Reference Database Number 69, edited by P. J. Linstrom and W. G. Mallard (NIST, Gaithersburg, MD, 2023).
- ⁵³B. Lafaurie, C. Nardone, R. Scardovelli, S. Zaleski, and G. Zanetti, "Modelling merging and fragmentation in multiphase flows with SURFER," *J. Comput. Phys.* **113**, 134–147 (1994).
- ⁵⁴R. I. Issa, "Solution of the implicitly discretised fluid flow equations by operator-splitting," *J. Comput. Phys.* **62**, 40–65 (1986).
- ⁵⁵S. V. Patankar, *Numerical Heat Transfer and Fluid Flow*, *Electro Skills Series* (Hemisphere Publishing Corporation, 1980).
- ⁵⁶D. L. Youngs, "Time-dependent multi-material flow with large fluid distortion," in *Numerical Methods in Fluid Dynamics*, edited by K. W. Morton and M. J. Baines (Academic Press, 1982), Vol. 24, pp. 273–285.
- ⁵⁷J. Eggers and E. Villermaux, "Physics of liquid jets," *Rep. Prog. Phys.* **71**, 036601 (2008).
- ⁵⁸P. Koukouvini, M. Gavaises, O. Supponen, and M. Farhat, "Simulation of bubble expansion and collapse in the vicinity of a free surface," *Phys. Fluids* **28**(5), 052103 (2016).
- ⁵⁹C. Clanet, "Waterbells and Liquid Sheets," *Annu. Rev. Fluid Mech.* **39**, 469–496 (2007).
- ⁶⁰P. A. Quinto-Su and K. Ando, "Nucleating bubble clouds with a pair of laser-induced shocks and bubbles," *J. Fluid Mech.* **733**, R3 (2013).
- ⁶¹C. Lechner, W. Lauterborn, M. Koch, and R. Mettin, "Fast, thin jets from bubbles expanding and collapsing in extreme vicinity to a solid boundary: A numerical study," *Phys. Rev. Fluids* **4**, 21601 (2019).
- ⁶²D. Obreschkow, P. Kobel, N. Dorsaz, A. de Bosset, C. Nicollier, and M. Farhat, "Cavitation bubble dynamics inside liquid drops in microgravity," *Phys. Rev. Lett.* **97**, 094502 (2006).
- ⁶³B. J. McBride, M. J. Zehe, and S. Gordon, *NASA Glenn Coefficients for Calculating Thermodynamic Properties of Individual Species* (John H. Glenn Research Center at Lewis Field, 2002), p. 295.
- ⁶⁴J. Chandran R and A. Salih, "A modified equation of state for water for a wide range of pressure and the concept of water shock tube," *Fluid Phase Equilib.* **483**, 182–188 (2019).
- ⁶⁵F. Denner, "The Gilmore-NASG model to predict single-bubble cavitation in compressible liquids," *Ultrason. Sonochem.* **70**, 105307 (2021).